13. Shirakashi R, Tanasawa I. 1998. Method of designing prefreezing protocol in cryopreservation of biological materials. Ann N Y Acad Sci 858:175–182.
14. Mathias SF, Franks F, Hatley RH. 1985. Preservation of viable cells in the undercooled state. Cryobiology 22:537–546.
15. Siow LF, Rades T, Lim MH. 2007. Characterizing the freezing behavior of liposomes as a tool to understand the cryopreservation procedures. Cryobiology 55:210–221.
16. Siow LF, Rades T, Lim MH. 2008. Cryo-responses of two types of large unilamellar vesicles in the presence of non-permeable or permeable cryoprotecting agents. Cryobiology 57:276–285.
17. Talsma H, Van Steenbergen MJ, Crommelin DJ. 1992. The cryopreservation of liposomes. 2. Effect of particle size on crystallization behavior and marker retention. Cryobiology 29:80–86.
18. Charoenrein S, Reid DS. 1989. The use of DSC to study the kinetics of heterogeneous and homogeneous nucleation of ice in aqueous systems. Thermochim Acta 156:373–381.
19. Seki S, Kleinhans FW, Mazur P. 2009. Intracellular ice formation in yeast cells vs. cooling rate: Predictions from modeling vs. experimental observations by differential scanning calorimetry. Cryobiology 58:157–165.
20. Bronshteyn VL, Steponkus PL. 1993. Calorimetric studies of freeze-induced dehydration of phospholipids. Biophys J 65:1853–1865.
21. Lefevre T, Toscani S, Picquart M, Dugue J. 2002. Crystallization of water in multilamellar vesicles. Eur Biophys J 31:126–135.
22. Siminovitch D, Chapman D. 1971. Liposome bilayer model systems of freezing living cells. FEBS Lett 16:207–212.
23. Talsma H, Steenbergen MJV, Crommelin DJA. 1991. The cryopreservation of liposomes: 3. Almost complete retention of a water-soluble marker in small liposomes in a cryoprotectant containing dispersion after a freezing/thawing cycle. Int J Pharm 77:119–126.
24. Harrigan PR, Madden TD, Cullis PR. 1990. Protection of liposomes during dehydration or freezing. Chem Phys Lipids 52:139–149.
25. Higgins J, Hodges NA, Olliff CJ, Phillips AJ. 1986. Factors influencing cryoprotective activity and drug leakage from liposomes after freezing. J Pharm Pharmacol 38:259–263.
26. Hupfeld S, Moen HH, Ausbacher D, Haas H, Brandl M. 2010. Liposome fractionation and size analysis by asymmetrical flow field-flow fractionation/multi-angle light scattering: Influence of ionic strength and osmotic pressure of the carrier liquid. Chem Phys Lipids 163:141–147.
27. Ohtake S, Schebor C, Palecek SP, de Pablo JJ. 2005. Phase behavior of freeze-dried phospholipid-cholesterol mixtures stabilized with trehalose. Biochim Biophys Acta 1713:57–64.
28. Talsma H, van Steenbergen MJ, Salemink PJ, Crommelin DJ. 1991. The cryopreservation of liposomes. 1. A differential scanning calorimetry study of the thermal behavior of a liposome dispersion containing mannitol during freezing/thawing. Pharm Res 8:1021–1026.
29. MacDonald RC, MacDonald RI, Menco BP, Takeshita K, Subbarao NK, Hu LR. 1991. Small-volume extrusion apparatus for preparation of large, unilamellar vesicles. Biochim Biophys Acta 1061:297–303.
30. Kristiansen J. 1992. Leakage of a trapped fluorescent marker from liposomes: Effects of eutectic crystallization of NaCl and internal freezing. Cryobiology 29:575–584.
31. Bartlett GR. 1959. Phosphorus assay in column chromatography. J Biol Chem 234:466–468.
32. Kaasgaard T, Mouritsen OG, Jørgensen K. 2003. Freeze/thaw effects on lipid-bilayer vesicles investigated by differential scanning calorimetry. Biochim Biophys Acta 1615:77–83.
33. Wu WG, Chi LM, Yang TS, Fang SY. 1991. Freezing of phosphocholine headgroup in fully hydrated sphingomyelin bilayers and its effect on the dynamics of nonfreezable water at subzero temperatures. J Biol Chem 266:13602–13606.
34. Rall WF, Mazur P, McGrath JJ. 1983. Depression of the ice-nucleation temperature of rapidly cooled mouse embryos by glycerol and dimethyl sulfoxide. Biophys J 41:1–12.
35. Nagle JF, Wilkinson DA. 1978. Lecithin bilayers. Density measurement and molecular interactions. Biophys J 23:159–319.
36. Koster KL, Lei YP, Anderson M, Martin S, Bryant G. 2000. Effects of vitrified and nonvitrified sugars on phosphatidylcholine fluid-to-gel phase transitions. Biophys J 78:1932–1946.
37. Mui BL, Cullis PR, Evans EA, Madden TD. 1993. Osmotic properties of large unilamellar vesicles prepared by extrusion. Biophys J 64:443–453.
38. Akers MJ, Vasudevan V, Stickelmeyer M. 2002. Formulation development of protein dosage forms. Pharm Biotechnol 14:47–127.
39. Nail SL, Jiang S, Chongprasert S, Knopp SA. 2002. Fundamentals of freeze-drying. Pharm Biotechnol 14:281–360.
40. Blok MC, van Deenen LL, De Gier J. 1976. Effect of the gel to liquid crystalline phase transition on the osmotic behaviour of phosphatidylcholine liposomes. Biochim Biophys Acta 433:1–12.
41. Pencer J, White GF, Hallett FR. 2001. Osmotically induced shape changes of large unilamellar vesicles measured by dynamic light scattering. Biophys J 81:2716–2728.
42. Suzuki T, Komatsu H, Miyajima K. 1996. Effects of glucose and its oligomers on the stability of freeze-dried liposomes. Biochim Biophys Acta 1278:176–182.
43. Grabielle-Madelmont C, Perron R. 1983. Calorimetric studies on phospholipid-water systems: II. Study of water behavior. J Colloid Interface Sci 95:483–493.
44. Hubel A, Darr TB, Chang A, Dantzig J. 2007. Cell partitioning during the directional solidification of trehalose solutions. Cryobiology 55:182–188.
45. Ohtake S, Schebor C, de Pablo JJ. 2006. Effects of trehalose on the phase behavior of DPPC-cholesterol unilamellar vesicles. Biochim Biophys Acta 1758:65–73.

International Journal of Pharmaceutics 407 (2011) 111–118

Contents lists available at ScienceDirect

International Journal of Pharmaceutics

journal homepage: www.elsevier.com/locate/ijpharm

Differences in crystallization rate of nitrendipine enantiomers in amorphous solid dispersions with HPMC and HPMCP

Tamaki Miyazaki[a,*], Yukio Aso[a], Sumie Yoshioka[b], Toru Kawanishi[a]

[a] Division of Drugs, National Institute of Health Sciences, 1-18-1 Kamiyoga, Setagaya-ku, Tokyo 158-8501, Japan
[b] School of Pharmacy, University of Connecticut, Storrs, CT, United States

ARTICLE INFO

Article history:
Received 21 October 2010
Received in revised form
21 December 2010
Accepted 19 January 2011
Available online 26 January 2011

Keywords:
Nitrendipine
Enantiomer
Chiral polymer
Solid dispersions
Crystallization

ABSTRACT

To clarify the contribution of drug–polymer interaction to the physical stability of amorphous solid dispersions, we studied the crystallization rates of nitrendipine (NTR) enantiomers with identical physicochemical properties in the presence of hydroxypropylmethylcellulose (HPMC), hydroxypropylmethylcellulose phthalate (HPMCP) and polyvinylpyrrolidone (PVP). The overall crystallization rate at 60 °C and the nucleation rate at 50–70 °C of (+)-NTR were lower than those of (−)-NTR in the presence of 10–20% HPMC or HPMCP. In contrast, similar crystallization profiles were observed for the NTR enantiomers in solid dispersions containing PVP. The similar glass transition temperatures for solid dispersions of (−)-NTR and (+)-NTR suggested that the molecular mobility of the amorphous matrix did not differ between the enantiomers. These results indicate that the interaction between the NTR enantiomers and HPMC or HPMCP is stereoselective, and that differences in the stereoselective interaction create differences in physical stability between (−)-NTR and (+)-NTR at 50–70 °C. However, no difference in physical stability between the enantiomers was obvious at 40 °C. Loss of the difference in physical stability between the NTR enantiomers suggests that the stereoselective interaction between NTR and the polymers may not contribute significantly to the physical stabilization of amorphous NTR at 40 °C.

1. Introduction

Nifedipine analogues are used for treatment of cardiovascular disorders. Most of them are poorly water soluble and their bioavailability is low when administered orally in crystal form. To improve the bioavailability by increasing the dissolution rate and solubility, amorphous solid dispersions of nifedipine analogues have been studied over the past few decades (Suzuki and Sunada, 1998; Chutimaworapan et al., 2000; Vippagunta et al., 2002; Hirasawa et al., 2003a,b, 2004; Tanno et al., 2004; Karavas et al., 2005, 2006; Wang et al., 2005, 2007; Kim et al., 2006; Konno and Taylor, 2006; Huang et al., 2008; Marsac et al., 2008; Rumondor et al., 2009a,b). Drugs in an amorphous state are more easily dissolved in water than their crystalline counterparts. However, recrystallization to a thermodynamically stable form during long-term storage is a matter of concern. The physical stability of amorphous solid dispersions (crystallization tendency) has been reported to correlate with several factors, such as molecular mobility (Aso et al., 2004; Miyazaki et al., 2007), drug–excipient interactions and miscibility (Matsumoto and Zografi, 1999; Marsac et al., 2006, 2009; Miyazaki et al., 2004, 2006, 2007; Konno and Taylor, 2006; Haddadin et al., 2009; Tao et al., 2009; Telang et al., 2009). The crystallization rate of amorphous nitrendipine (NTR) increases with a decrease in the glass transition temperature (T_g) associated with water sorption, indicating that molecular mobility, in terms of T_g, is correlated with physical stability. However, amorphous nilvadipine is more stable than nifedipine, even though the two had similar T_g values, indicating that the difference in physical stability between nilvadipine and nifedipine might be attributable to differences in chemical structure (Miyazaki et al., 2007). Hydrogen bond interaction between felodipine and hydroxypropylmethylcellulose (HPMC) or hydroxypropylmethylcellulose acetate succinate is considered to decrease the nucleation rate of felodipine, since no significant change in molecular mobility, reflected in T_g value, has been observed (Konno and Taylor, 2006). Also, drug–excipient miscibility is reportedly related to the physical stability of nifedipines. Drug crystallization has been observed to occur earlier in solid dispersions showing phase separation due to low miscibility of the drug with the excipient polymers (Rumondor et al., 2009a,b; Marsac et al., 2010). In order to develop stable amorphous solid dispersions, it is important to clarify the relative significance of these factors for the physical stability of amorphous solid dispersions. Therefore, designing a model system that is as simple as possible is the key to evaluation of each individual factor.

NTR has an asymmetric carbon (Fig. 1), and is available as a mixture of both enantiomers. These enantiomers can be resolved by chiral chromatography. Since both enantiomers have identical physical and chemical properties, including molecular mass, T_g,

* Corresponding author. Tel.: +81 3 3700 1141; fax: +81 3 3707 6950.
E-mail address: miyazaki@nihs.go.jp (T. Miyazaki).

0378-5173/$ – see front matter © 2011 Elsevier B.V. All rights reserved.
doi:10.1016/j.ijpharm.2011.01.035

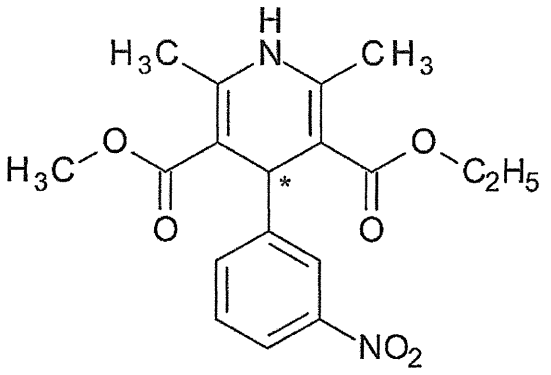

Fig. 1. Chemical structure of NTR. The asterisk represents asymmetric carbon.

melting point and density, the effects of molecular mobility and chemical structure on their physical stability are expected to be the same. Therefore, solid dispersions of NTR enantiomers may provide a useful model system for studies of drug–polymer stereoselective interaction. In the present study, HPMC and hydroxypropylmethylcellulose phthalate (HPMCP) were used as chiral polymers, and polyvinylpyrrolidone (PVP), an achiral polymer, was selected as a control to investigate the effect of drug–polymer interaction on the physical stability of amorphous NTR enantiomers. The overall crystallization rates were determined from the time-profiles of amorphous drug remaining, as measured by differential scanning calorimetry (DSC). Furthermore, the nucleation and the crystal growth rates of each NTR enantiomer in the solid dispersions containing HPMC, HPMCP or PVP were determined by polarized light microscopy. Measurements of T_g and Fourier-transform infrared spectra (FT-IR) were carried out for evaluation of molecular mobility and drug–polymer interactions, respectively.

2. Materials and methods

2.1. Materials

PVP (PVP10) and HPMC (USP grade) were purchased from Sigma–Aldrich, Inc. HPMCP (HP-55) was kindly obtained from Shin-Etsu Chemical Co., Ltd.

NTR (Wako Pure Chemical Industries Ltd.) was resolved on a CHIRALCEL OJ-H column (Daicel Chemical Industries, Ltd., 10 mm × 250 mm) into two fractions of each enantiomer with a mobile phase of n-hexane/ethanol (100/15, flow rate: 4 ml/min). A 500 μl of 1% NTR solution in n-hexane/ethanol (1/1) was injected, and ultraviolet spectrophotometric detection was carried out at 254 nm. The circular dichroism spectrum of the first fraction exhibited a negative peak at around 360 nm, and the second one exhibited a positive peak. Therefore, the first and second fractions of NTR were designated (−)-NTR and (+)-NTR, respectively. The optical purity of each enantiomer was determined to be more than 99.96%, and the amount of photo degradation product of NTR was determined to be less than 0.03% by liquid chromatography, on a CHIRALCEL OJ-H column (Daicel Chemical Industries, Ltd.,

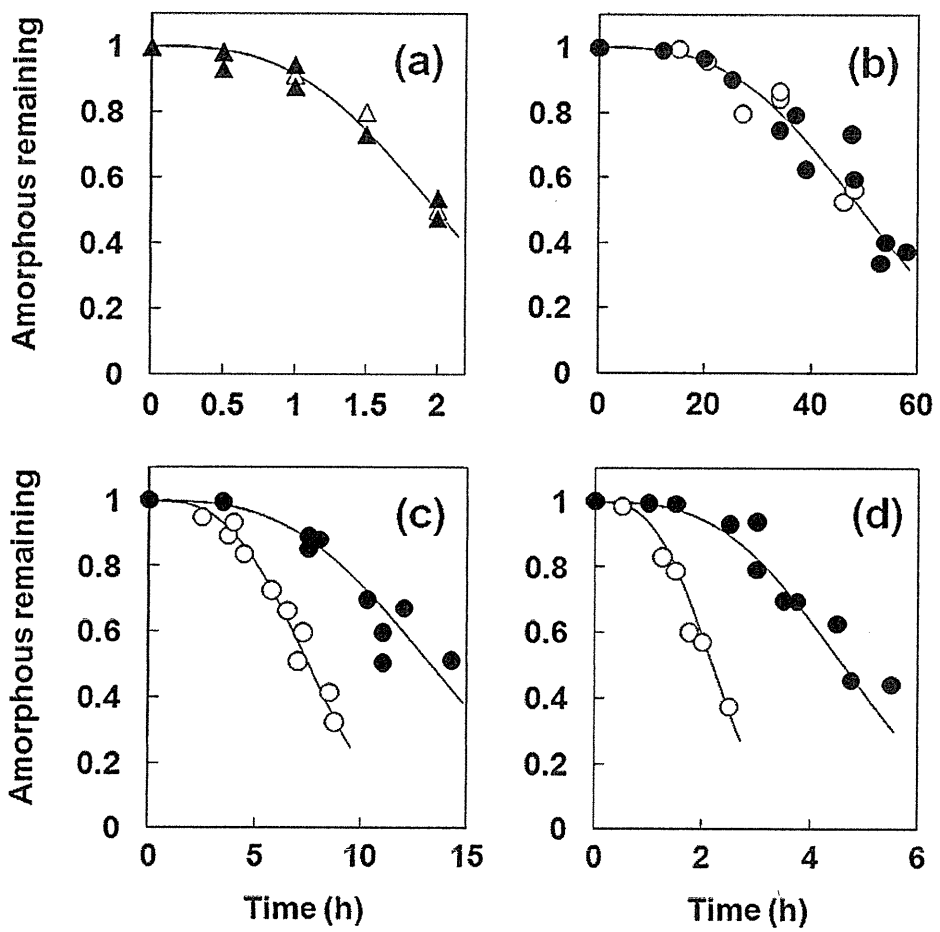

Fig. 2. Crystallization profiles of each NTR enantiomer alone ((a); △, ▲) and the enantiomers in solid dispersions (○, ●) with (b) 10% PVP, (c) 10% HPMC and (d) 10% HPMCP at 60 °C. Open symbols represent (−)-NTR and solid symbols represent (+)-NTR. The lines in the figures represent the best fit of the Avrami equation.

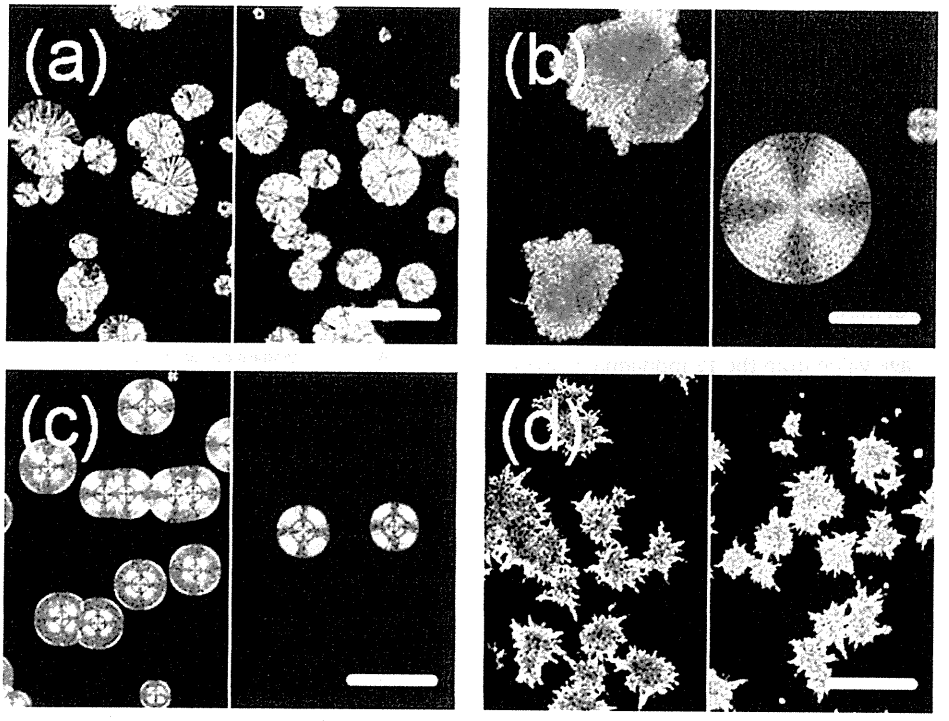

Fig. 3. Typical crystal shape observed for the amorphous NTR enantiomers and their solid dispersions: (a) without polymer, (b) 10% HPMC, (c) 10% HPMCP and (d) 10% PVP. The left side of each micrograph was taken from the (−)-NTR samples, and the right side from the (+)-NTR samples. The bars in the micrographs correspond to 100 μm.

4.6 mm × 250 mm) with a mobile phase of n-hexane/ethanol = 10/1 (1 ml/min). Since NTR is a photo sensitive compound, NTR samples were handled under dim light (<120 lx).

2.2. Determination of the overall crystallization rate of amorphous NTR enantiomers

Amorphous solid dispersions of the NTR enantiomers were prepared by melt-quenching drug–polymer mixtures. One NTR enantiomer and a polymer were initially dissolved in a solvent that was suitable for both components. Ethanol/acetone (1:1) was used for the NTR–HPMC and NTR–HPMCP combinations, and ethanol was used for the NTR–PVP combination. Next, the solvent was rotary-evaporated to obtain a homogeneous drug–polymer mixture. Approximately 4 mg of the pulverized mixture was weighed into an aluminum pan for DSC, and was kept at around 180 °C in the cell of a DSC (DSC2920, TA Instruments) for approximately 2 min under dry nitrogen gas flow (30 ml/min). The melted sample was transferred to a desiccator containing phosphorus pentoxide, and the desiccator was stored at a constant temperature of 30–70 °C. For the pure NTR enantiomer, the resolved enantiomer crystal (4 mg) was melt-quenched as described above to obtain an amorphous sample.

After certain periods of time, the change in heat capacity (ΔC_p) at T_g was measured for the stored amorphous samples by DSC at a heating rate of 20 °C/min. The amount of amorphous drug remaining in the sample at time t, $x(t)$, was calculated according to Eq. (1):

$$x(t) = \frac{\Delta C_{pt}}{\Delta C_{p0}} \quad (1)$$

where ΔC_{pt} and ΔC_{p0} are the ΔC_p values at time t and initially, respectively. The time required for 10% of the amorphous NTR to crystallize (t_{90}) was estimated as an indicator of the crystallization tendency. The time-profiles of $x(t)$ were analyzed according to the Avrami equation (Eq. (2), $n = 3$) to calculate t_{90}:

$$x(t) = \exp[-kt^n] \quad (2)$$

where k is the crystallization rate constant and n is the Avrami index. HPLC analysis of stored NTR samples showed no evidence of degradation during melt-quenching and subsequent storage.

2.3. Determination of nucleation rate and crystal growth rate of NTR enantiomer

The nucleation rate and the crystal growth rate were determined for samples prepared in a space between two glass disks separated by a stainless steel ring. The NTR enantiomer–polymer mixture, which was described above, or the crystalline NTR enantiomer (1.5–2 mg) was placed on a clean glass disk (thickness: 0.12 mm, diameter: 16 mm) and heated at 180 °C in the DSC with a stainless steel ring (inner diameter: 6 mm, thickness: 20 μm) as a spacer. After the sample had melted completely, it was covered with another glass disk (thickness: 0.12 mm, diameter: 12 mm) to yield an amorphous layer between the glasses. Attention was paid to ensure that the layer was free of bubbles. For measurements at temperatures above 40 °C, the sample was stored in the chamber of a heating/cooling stage for microscopy (THMS600, Linkam Scientific Instruments), which had been adjusted to a prescribed temperature in advance. The moisture in the chamber was removed by purging with dry nitrogen gas for 10–15 min. Microscopic images of the sample were recorded at appropriate time intervals by a digital camera (DXM1200F, Nikon Corporation) attached to a polarized light microscope (ECLIPSE E600 POL, Nikon Corporation) with a 10× objective lens. In order to minimize possible photo degradation of NTR by the polarized light, the light source of the microscope was shut off when images were not recorded. For measurements at 30 °C, the samples were stored at 30 °C in desiccators containing phosphorous pentoxide. After an appropriate period of storage, microscopic images of the sample were recorded, and the sample was again stored at 30 °C in a dry state.

2.3.1. Measurement of nucleation rate

The nucleation rate of the NTR enantiomers was estimated from time-profiles of nucleation site density determined from microscopic images of the stored samples. Nucleation site density per unit volume was calculated from the number of nucleation sites per unit area and the depth of field of the lens used for data collection. The depth of field was calculated to be 8.46 μm from the wavelength of the light (546 nm) and the numerical aperture of the lens (0.25). For samples with more than a dozen nucleation sites per fixed field at the end of the observation period, nucleation sites were counted in one fixed field. For samples with less than a dozen nucleation sites per field near the end of the observation period, and those stored at 30 °C, nucleation sites were counted for 12 individual areas in one sample, and the average value from the 12 individual images was regarded as the number of nucleation sites per field. The nucleation rate was obtained from the slope of time-profiles of the number of nucleation sites per unit volume (nucleation site density) at steady state. In cases showing preferential nucleation and growth at the sample periphery, these sites were not included in the analysis. The reported nucleation rates were average values of those obtained for at least three samples prepared separately.

2.3.2. Measurement of crystal growth rate

The crystal growth rates at temperatures above 40 °C were measured concurrently with the nucleation rate measurements as described above. The measurements at 30 °C were carried out using samples that showed more than a dozen nucleation sites per one field after a few months of storage in desiccators containing phosphorous pentoxide. The sample was placed in the chamber of the heating/cooling stage controlled at 30 °C, and the growth of crystals was observed in a fixed field. The radius of each crystal was estimated from a circular approximation by using Lumina Vision software (Mitani Co.). The average crystal growth rate was calculated from the increase in the radius as a function of time based on observations of at least 20 crystals.

2.4. FT-IR

FI-IR spectra were collected using a FT/IR-6300 (JASCO Corporation) by the KBr method at ambient room temperature. Transmission spectra were obtained for KBr disks containing 1–1.5% sample at a resolution of 0.4 cm^{-1} within the range of 4000–400 cm^{-1}. An accumulation of 128–256 scans was acquired for each disk.

3. Results

3.1. Effects of polymers on the overall crystallization rates of NTR enantiomers in solid dispersions

No significant differences in the melting point (158 °C), T_g (33 °C) and ΔC_p at T_g (0.40 J/g/K) were observed between (−)-NTR and (+)-NTR. Table 1 shows the T_g values of amorphous solid dispersions of (−)-NTR and (+)-NTR. There appeared to be no significant difference in the T_g values between the two. The solid dispersions containing HPMC (10–20%) and 5% PVP showed T_g values similar to that of each NTR enantiomer alone. T_g values for solid dispersions containing 10% PVP were slightly higher than that of each NTR enantiomer alone, whereas solid dispersions containing HPMCP (10–20%) exhibited T_g values slightly lower than that of each NTR enantiomer alone.

Fig. 2 shows time-profiles of overall crystallization of NTR enantiomers at 60 °C. No significant differences in the overall crystallization profiles were observed between (−)-NTR and (+)-NTR without polymer (Fig. 2(a)), and between (−)-NTR and (+)-NTR in solid dispersions containing 10% PVP (Fig. 2(b)). In contrast, differences in time-profiles between the enantiomers were observed for solid dispersions containing 10% HPMC or HPMCP: (+)-NTR crystallized more slowly than (−)-NTR, as shown in Fig. 2(c) and (d). Table 2 shows the t_{90} values for the amorphous NTR enantiomers obtained for NTR alone and NTR in the solid dispersions. The t_{90} values for (−)-NTR without polymer and those of solid dispersions containing 5–10% PVP were almost the same as the t_{90} values for (+)-NTR without polymer and those of solid dispersions containing 5–10% PVP, respectively, at the temperatures studied. The t_{90} values at 50 and 60 °C for (+)-NTR were 1.5–2.0 times longer than that for (−)-NTR in solid dispersions containing 10–20% HPMC or HPMCP. At 40 °C, however, any difference between the enantiomers was not clear.

Table 1
T_g of pure NTR enantiomers and their solid dispersions with a polymer.

Polymer	Polymer content [%]	T_g[a] [°C]	
		(−)-NTR	(+)-NTR
None	0	33.2 ± 0.1	33.1 ± 0.2
HPMC	10	33.1 ± 1.0	33.0 ± 0.7
	20	33.1 ± 0.8	33.0 ± 0.7
HPMCP	10	31.2 ± 0.7	31.0 ± 0.4
	20	30.8 ± 1.2	30.5 ± 0.9
PVP	5	33.0 ± 0.2	33.1 ± 0.2
	10	36.3 ± 1.2	36.2 ± 0.8

[a] Average ± standard deviation ($n = 3$).

3.2. Effects of polymers on the nucleation rate and crystal growth rate

Fig. 3 shows the typical micrographs of NTR crystals grown from amorphous pure enantiomers and their solid dispersions with a polymer. The recrystallized NTR enantiomers without polymers showed a melting point of 158 °C, suggesting the same crystal form as the originally resolved stable one. The melting point of the samples containing 10% HPMC, HPMCP and PVP was approximately 151 °C in all cases, regardless of the various crystal shapes shown in Fig. 3. The difference from the melting point of the pure enantiomers would have been due to melting point depression by the

Table 2
t_{90} for NTR enantiomers with and without polymer.

Temperature [°C]	Polymer	[%]	t_{90}[a] [h]			
			(−)-NTR		(+)-NTR	
40	None	0	41	(1)	41	(1)
	HPMC	10	230, 240[b]		230, 230[b]	
	HPMCP	10	49	(1)	49	(1)
50	None	0	5.7	(0.2)	5.7	(0.1)
	PVP	10	250	(10)	240	(4)
	HPMC	10	17	(0.4)	25	(0.1)
	HPMCP	10	6.1	(0.3)	11	(0.3)
60	None	0	1.1	(0.1)	1.1	(0.1)
	PVP	5	3.5	(0.1)	3.6	(0.1)
		10	25 ± 3[c]		25 ± 3[c]	
	HPMC	10	3.8, 4.1[b]		6.7, 6.9[b]	
		20	8.7	(0.3)	15	(0.4)
	HPMCP	10	1.5 ± 0.2[c]		2.7 ± 0.3[c]	
		20	3.2	(0.1)	6.4	(0.2)

[a] The values in parentheses are standard error estimated from single experiments using Origin 8.1 software (Lightstone Corp.).
[b] Results with two values represent the results obtained from duplicate experiments using separately prepared samples.
[c] Mean ± standard deviation ($n = 3$).

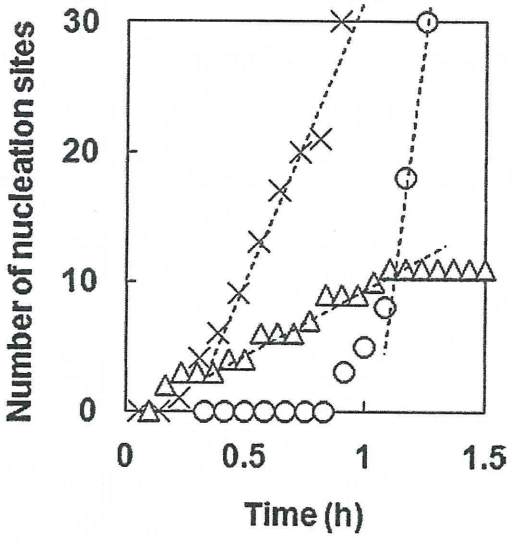

Fig. 4. Time profiles of the number of nucleation sites per field of view for (+)-NTR at 50 °C (○), 60 °C (×) and 70 °C (△). The dotted lines show the linear regression at steady state.

added polymers, as the melting point fell gradually with increasing polymer content (data not shown). The data suggested that differences in crystal habit, rather than polymorphism, might have been responsible for the differences in crystal shape among the solid dispersions.

Fig. 4 shows the typical time-profiles of the nucleation of amorphous NTR enantiomer stored at various temperatures. The lower the storage temperature, the longer the period required before the first crystal was observed. The nucleation rates at steady state were obtained from the slope of the lines in Fig. 4, and these were plotted against storage temperature (Fig. 5). As expected from the similar overall crystallization profiles of the NTR enantiomers (Fig. 2(a) and (b)), no significant difference in the nucleation rates between (−)-NTR and (+)-NTR was observed for amorphous NTR alone and the solid dispersions containing PVP within the temperature range studied (Fig. 5(a)). In contrast, the nucleation rates of (+)-NTR were lower than those of (−)-NTR in the solid dispersions containing HPMC and HPMCP (Fig. 5(b)) within the temperature range of 50–70 °C. At 40 °C, however, the differences in the rates between (−)-NTR and (+)-NTR were not pronounced. These results were consistent with the t_{90} values of the enantiomers shown in Table 2.

Fig. 6 shows the typical time-profiles of the NTR crystal growth at 60 °C. Crystal radius increased linearly with time, and the growth rate was estimated from linear regression of the plots. The higher the temperature, the faster the crystals grew within the temperature range studied (Fig. 7). In contrast to the nucleation rates, no significant growth rate differences between the NTR enantiomers were observed, irrespective of the absence or presence of any polymer.

3.3. FT-IR

FT-IR spectra (4000–400 cm^{-1}) of (−)-NTR and (+)-NTR were indistinguishable from one another for both the amorphous and the crystalline forms. Similarly, the FT-IR spectra of amorphous solid dispersions were almost the same for (−)-NTR and (+)-NTR with any polymer. Fig. 8 shows the spectra for crystalline (−)-NTR (dotted line in Fig. 8 (a)), NTR solid dispersions containing 25–75% HPMC and HPMC alone (dotted line in Fig. 8 (c)) in the range of 1800–1550 cm^{-1}, corresponding to C=O stretching region of NTR. Spectra with and without an asterisk represent that of (−)-NTR

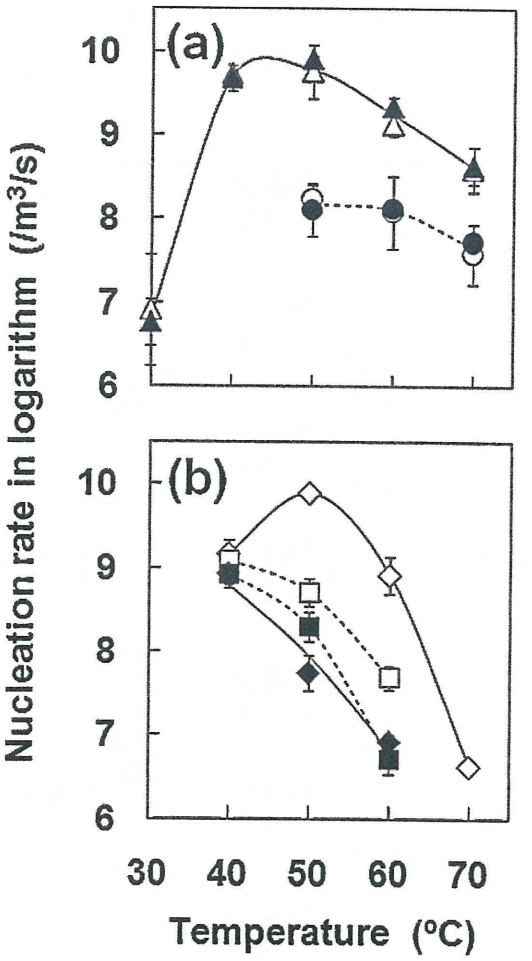

Fig. 5. Plots of nucleation rate as a function of temperature. Error bars represent standard deviation for at least triplicate experiments. (a) △, ▲: without polymer, ○, ●: 10% PVP and (b) □, ■: 10% HPMC, ◇, ◆: 10% HPMCP. Open symbols represent (−)-NTR and solid symbols represent (+)-NTR.

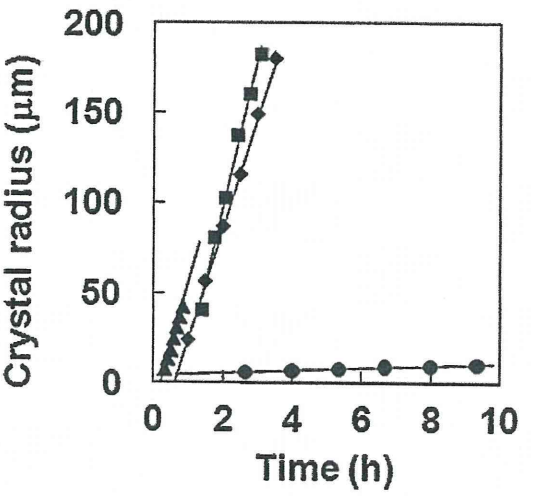

Fig. 6. Typical time profiles of the radius of NTR crystals in (+)-NTR alone (▲), and solid dispersions with 10% HPMC (■), 10% HPMCP (◆) and 10% PVP (●) at 60 °C.

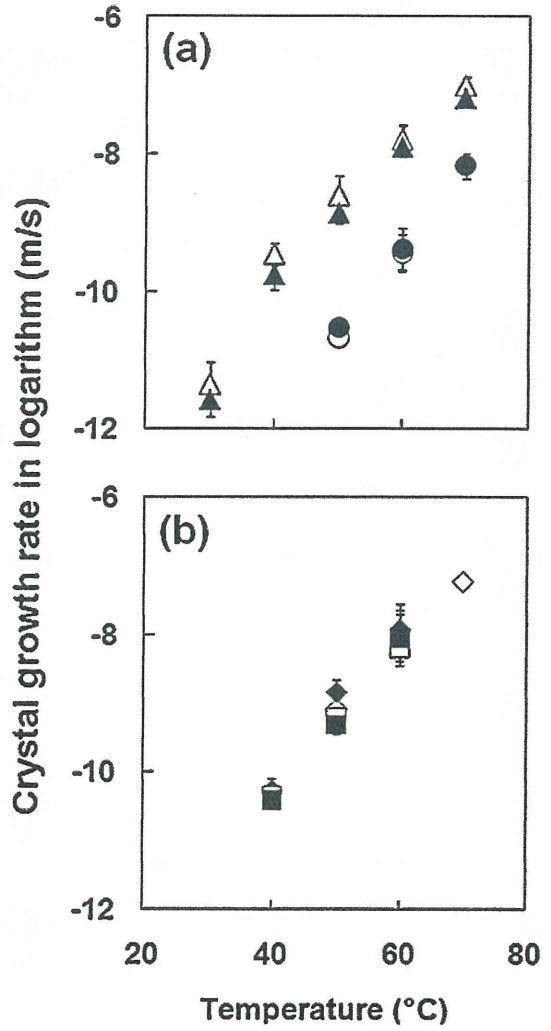

Fig. 7. Temperature dependence of crystal growth rate of NTR enantiomers. Error bars represent standard deviation for at least triplicate experiments. (a) △, ▲: without polymer; ○, ●: 10% PVP and (b) □, ■: 10% HPMC; ◇, ◆: 10% HPMCP. Open symbols represent (−)-NTR and solid symbols represent (+)-NTR.

and (+)-NTR, respectively. Despite its vicinity to the asymmetric carbon, carbonyl group of (−)-NTR and (+)-NTR showed same spectra even in the presence of HPMC. Likewise, no difference in spectra between solid dispersions of (−)-NTR and (+)-NTR containing HPMCP was observed (data not shown).

Fig. 9 shows the spectra in the range of 3650–3150 cm^{-1}, corresponding to NH stretching vibrations of nifedipine derivatives (Konno and Taylor, 2006), where the changes in peak position were obvious upon mixing with polymers as solid dispersions. There were also no obvious differences in the spectra between the two enantiomers. The peak around 3350 cm^{-1} was assigned to the NH stretching vibration that was expected to be involved in the hydrogen bonding between the drug and a polymer. The peak position was shifted from 3360 cm^{-1} to 3337 cm^{-1} by amorphization, and additionally shifted to 3291 cm^{-1} in the presence of 50% PVP (Figs. 9(b) and 10). On the other hand, for solid dispersions prepared with HPMC and HPMCP, the peak position showed a degree of shift to a higher wavenumber (Figs. 9(c) and (d) and 10). The peak position for solid dispersions with 75% HPMCP was nearly equal to that of the pure NTR crystals. These changes in peak position showed the same tendency for both (+)-NTR and (−)-NTR.

4. Discussion

The overall crystallization of (−)-NTR proceeded faster than that of (+)-NTR in solid dispersions with HPMC or HPMCP (Fig. 2(c) and (d)), while that for solid dispersions with PVP proceeded at almost the same rate, regardless of NTR chirality (Fig. 2(b)). The nucleation rates of (−)-NTR were greater than those of (+)-NTR in solid dispersions with HPMC or HPMCP at 50–70 °C (Fig. 5(b)), while no difference in nucleation rates between the NTR enantiomers was observed for solid dispersions with PVP (Fig. 5(a)). The T_g values for samples using (−)-NTR or (+)-NTR were almost the same (Table 1), suggesting that the differences in the overall crystallization profiles and nucleation rates between the enantiomers are not due to differences in molecular mobility between (−)-NTR and (+)-NTR in solid dispersions with HPMC or HPMCP. The difference in physical stability between the two enantiomers may be explained by the difference in strength of NTR–polymer interaction between them. The results obtained from FT-IR measurements indicate that PVP interacts with NTR through hydrogen bonding at the NH moiety of NTR (Figs. 9 and 10). Almost the same degrees of shift in wavenumber for NH stretching suggest a similar strength of hydrogen bond interaction for (−)-NTR and (+)-NTR. PVP polymer chains possess an asymmetric carbon in a monomer unit, and are composed of monomer units with an equal ratio of R and S configurations. Therefore, (−)-NTR and (+)-NTR are considered to interact with PVP through hydrogen bonds of the same strength and number, resulting in a similar degree of physical stability between (−)-NTR and (+)-NTR. In contrast, HPMC and HPMCP are cellulose derivatives that are polymers of optically active D-glucose, and thus are expected to interact differently (strength and/or number) with NTR enantiomers, resulting in the difference in physical stability between (−)-NTR and (+)-NTR, although differences in interaction were not detectable by FT-IR. At 40 °C, however, the differences in physical stability between the enantiomers with HPMC or HPMCP were not remarkable (Table 2, Fig. 5). We do not have a satisfactory explanation for the loss of the difference in stabilization by HPMC and HPMCP. However, one possible explanation is as follows: The temperature dependence of the nucleation rate exhibits a maximum just above T_g because the nucleation rate is influenced by both molecular mobility and thermodynamic factors; an increase of temperature increases the molecular mobility, and thus the nucleation rate, whereas nucleation is thermodynamically favored at lower temperatures. A barrier due to molecular mobility is considered to play a predominant role in nucleation within the temperature range below the maximum point (Hancock and Zografi, 1997; Andronis and Zografi, 2000). Therefore, loss of the difference in physical stability between the enantiomers at 40 °C may be due to the predominant contribution of molecular mobility, since the molecular mobility is suggested to be similar for (−)-NTR and (+)-NTR in solid dispersions, as indicated by the T_g values (Table 1). However, physical stability data at temperatures below 40 °C, which are difficult to obtain within the commonly used experimental time scale, are needed in order to support this speculation.

In contrast to the nucleation rates, no significant difference in the crystal growth rates between the NTR enantiomers was observed for solid dispersions with HPMC or HPMCP (Fig. 7). The crystal growth rates for solid dispersions with HPMC or HPMCP were similar to those for each NTR enantiomer alone, indicating that the effects of HPMC and HPMCP on the crystal growth rate were small. This might be one of the reasons why differences in the crystal growth rate between the NTR enantiomers could not be detected in solid dispersions with HPMC or HPMCP.

It may be worth to note that PVP decreased the crystal growth rate of NTR enantiomers more than HPMC and HPMCP at all the temperatures studied (Fig. 7). On the other hand, PVP did not always decrease the nucleation rate of NTR more effectively than HPMC or

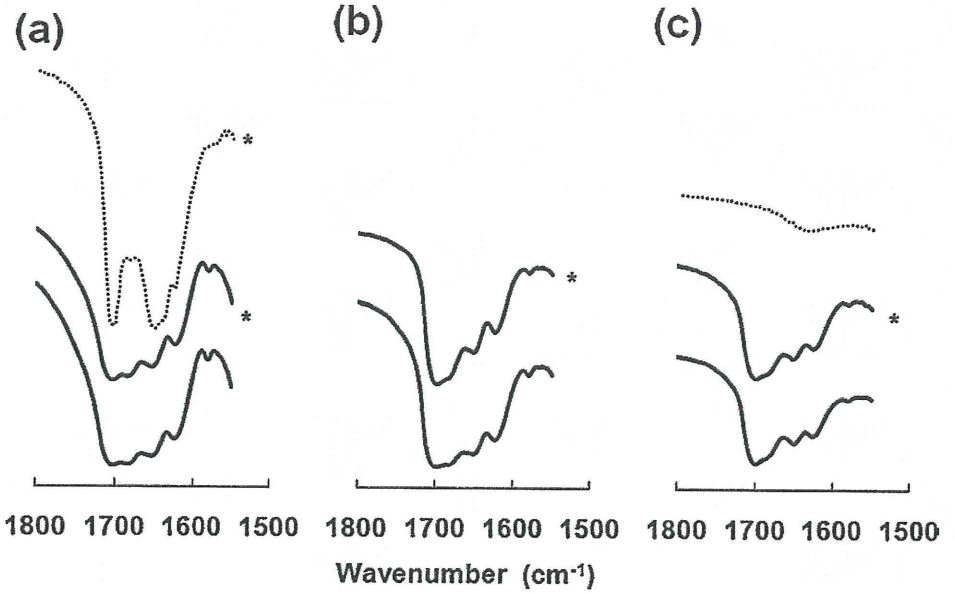

Fig. 8. FT-IR spectra of crystalline (−)-NTR, solid dispersions of NTR enantiomer containing HPMC, and HPMC alone. HPMC content was (a) 25% (b) 50%, and (c)75%. Dotted line in (a) represents the spectrum for crystalline (−)-NTR, and dotted line in (c) represents the spectrum for HPMC alone. The spectra with an asterisk are those of (−)-NTR.

HPMCP. For example, the nucleation rate of NTR at 60°C was following order; (−)-NTR, (+)-NTR ≈ (−)-NTR–HPMCP > (−)-NTR–PVP, (+)-NTR–PVP > (−)-NTR–HPMC > (+)-NTR–HPMC, (+)-NTR–HPMCP (Fig. 5). PVP seems to decrease the crystal growth rate more effectively than the nucleation rate of NTR, whereas HPMC and HPMCP decrease only the nucleation rate of NTR. The reason for the different stabilizing effects of the polymers for the nucleation and crystal growth of NTR is not clear. The growth rate of NTR may only be decreased by strong interactions such as hydrogen bonding between NTR and PVP, which is detectable by FT-IR (Figs. 9 and 10). Weak drug–polymer interactions, which are not detectable by FT-IR, may decrease the nucleation rate of NTR, as well as hydrogen bond interactions between drug and polymer.

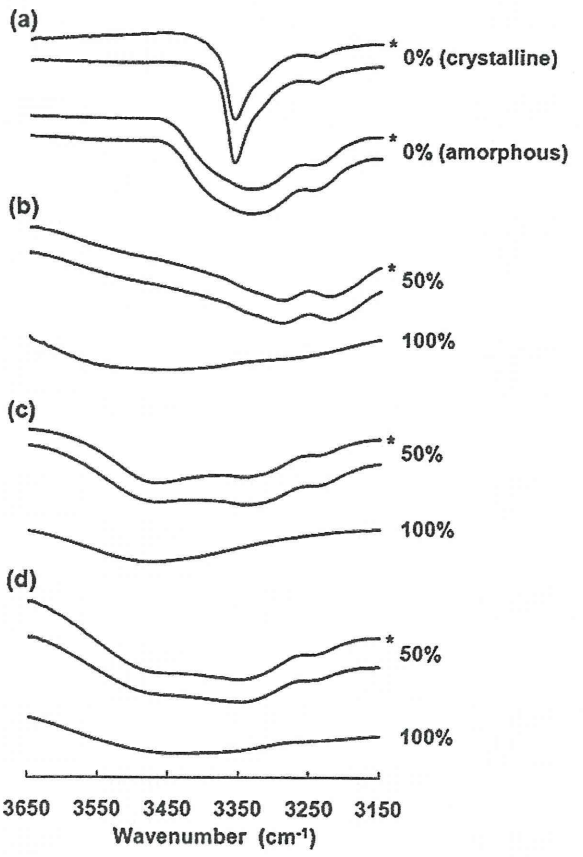

Fig. 9. FT-IR spectra of (a) crystalline and amorphous NTR enantiomers, and their amorphous solid dispersions with (b) PVP, (c) HPMC and (d) HPMCP. Percentages represent the weight percentage of polymer in the solid dispersions. The spectra with an asterisk are those of (−)-NTR.

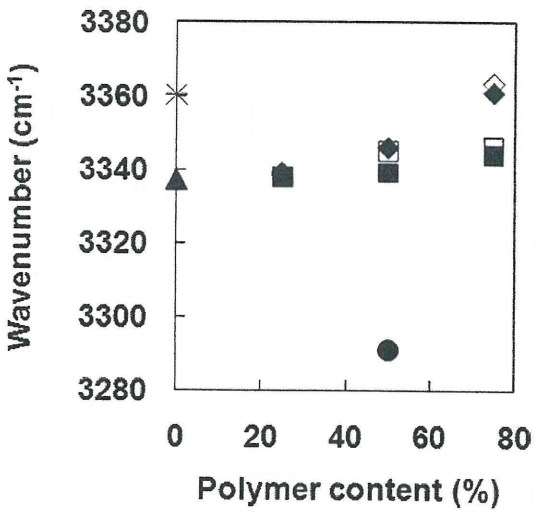

Fig. 10. Changes in FT-IR peak position showing the NH stretching region. +: (−)-NTR without polymer (crystalline); ×: (+)-NTR without polymer (crystalline); △, ▲: without polymer (amorphous); □, ■: HPMC; ◊, ◆: HPMCP; ○, ●: PVP. Open symbols represent (−)-NTR and solid symbols represent (+)-NTR.

5. Conclusions

Using NTR enantiomers as model drugs, the effects of stereoselective drug–polymer interaction on the crystallization rate of amorphous solid dispersions were elucidated. The chiral polymers, HPMC and HPMCP, retarded the crystallization of (+)-NTR more

effectively than that of (−)-NTR. The difference in physical stability at 50–70 °C would be due to stereoselective interaction. Stereoselective interaction affected the nucleation process more markedly than the crystal growth process. Since the stereoselective interaction between NTR enantiomers and HPMC or HPMCP would have been relatively weak, the impact of the interaction on the physical stability of amorphous NTR solid dispersions was obscure at room temperature.

Acknowledgements

Part of this work was supported by a Grant-in-aid for Research on Publicly Essential Drugs and Medical Devices from the Japan Health Sciences foundation.

References

Andronis, V., Zografi, G., 2000. Crystal nucleation and growth of indomethacin polymorphs from the amorphous state. J. Non-Cryst. Solids 271, 236–248.

Aso, Y., Yoshioka, S., Kojima, S., 2004. Molecular mobility-based estimation of the crystallization rates of amorphous nifedipine and phenobarbital in poly(vinylpyrrolidone) solid dispersions. J. Pharm. Sci. 93, 384–391.

Chutimaworapan, S., Ritthidej, G.C., Yonemochi, E., Oguchi, T., Yamamoto, K., 2000. Effect of water-soluble carriers on dissolution characteristics of nifedipine solid dispersions. Drug Dev. Ind. Pharm. 26, 1141–1150.

Haddadin, R., Qian, F., Desikan, S., Hussain, M., Smith, R.L., 2009. Estimation of drug solubility in polymers via differential scanning calorimetry and utilization of the fox equation. Pharm. Dev. Technol. 14, 18–26.

Hancock, B.C., Zografi, G., 1997. Characteristics and significance of the amorphous state in pharmaceutical systems. J. Pharm. Sci. 86, 1–12.

Hirasawa, N., Ishise, S., Miyata, H., Danjo, K., 2003a. Physicochemical characterization and drug release studies of nilvadipine solid dispersions using water-insoluble polymer as a carrier. Drug Dev. Ind. Pharm. 29, 339–344.

Hirasawa, N., Ishise, S., Miyata, H., Danjo, K., 2003b. An attempt to stabilize nilvadipine solid dispersion by the use of ternary systems. Drug Dev. Ind. Pharm. 29, 997–1004.

Hirasawa, N., Ishise, S., Miyata, H., Danjo, K., 2004. Application of nilvadipine solid dispersion to tablet formulation and manufacturing using crospovidone and methylcellulose as dispersion carriers. Chem. Pharm. Bull. 52, 244–247.

Huang, J., Wigent, R.J., Schwartz, J.B., 2008. Drug–polymer interaction and its significance on the physical stability of nifedipine amorphous dispersion in microparticles of an ammonio methacrylate copolymer and ethylcellulose binary blend. J. Pharm. Sci. 97, 251–262.

Karavas, E., Ktistis, G., Xenakis, A., Georgarakis, E., 2005. Miscibility behavior and formation mechanism of stabilized felodipine-polyvinylpyrrolidone amorphous solid dispersions. Drug Dev. Ind. Pharm. 31, 473–489.

Karavas, E., Ktistis, G., Xenakis, A., Georgarakis, E., 2006. Effect of hydrogen bonding interactions on the release mechanism of felodipine from nanodispersions with polyvinylpyrrolidone. Eur. J. Pharm. Biopharm. 63, 103–114.

Kim, E.J., Chun, M.K., Jang, J.S., Lee, I.H., Lee, K.R., Choi, H.K., 2006. Preparation of a solid dispersion of felodipine using a solvent wetting method. Eur. J. Pharm. Biopharm. 64, 200–205.

Konno, H., Taylor, L.S., 2006. Influence of different polymers on the crystallization tendency of molecularly dispersed amorphous felodipine. J. Pharm. Sci. 95, 2692–2705.

Marsac, P.J., Shamblin, S.L., Taylor, L.S., 2006. Theoretical and practical approaches for prediction of drug–polymer miscibility and solubility. Pharm. Res. 23, 2417–2426.

Marsac, P.J., Konno, H., Rumondor, A.C., Taylor, L.S., 2008. Recrystallization of nifedipine and felodipine from amorphous molecular level solid dispersions containing poly(vinylpyrrolidone) and sorbed water. Pharm. Res. 25, 647–656.

Marsac, P.J., Li, T., Taylor, L.S., 2009. Estimation of drug–polymer miscibility and solubility in amorphous solid dispersions using experimentally determined interaction parameters. Pharm. Res. 26, 139–151.

Marsac, P.J., Rumondor, A.C., Nivens, D.E., Kestur, U.S., Stanciu, L., Taylor, L.S., 2010. Effect of temperature and moisture on the miscibility of amorphous dispersions of felodipine and poly(vinyl pyrrolidone). J. Pharm. Sci. 99, 169–185.

Matsumoto, T., Zografi, G., 1999. Physical properties of solid molecular dispersions of indomethacin with poly(vinylpyrrolidone) and poly(vinylpyrrolidone-co-vinylacetate) in relation to indomethacin crystallization. Pharm. Res. 16, 1722–1728.

Miyazaki, T., Yoshioka, S., Aso, Y., Kojima, S., 2004. Ability of polyvinylpyrrolidone and polyacrylic acid to inhibit the crystallization of amorphous acetaminophen. J. Pharm. Sci. 93, 2710–2717.

Miyazaki, T., Yoshioka, S., Aso, Y., 2006. Physical stability of amorphous acetanilide derivatives improved by polymer excipients. Chem. Pharm. Bull. 54, 1207–1210.

Miyazaki, T., Yoshioka, S., Aso, Y., Kawanishi, T., 2007. Crystallization rate of amorphous nifedipine analogues unrelated to the glass transition temperature. Int. J. Pharm. 336, 191–195.

Rumondor, A.C., Marsac, P.J., Stanford, L.A., Taylor, L.S., 2009a. Phase behavior of poly(vinylpyrrolidone) containing amorphous solid dispersions in the presence of moisture. Mol. Pharm. 6, 1492–1505.

Rumondor, A.C.F., Ivanisevic, I., Bates, S., Alonzo, D.E., Taylor, L.S., 2009b. Evaluation of drug–polymer miscibility in amorphous solid dispersion systems. Pharm. Res. 26, 2523–2534.

Suzuki, H., Sunada, H., 1998. Influence of water-soluble polymers on the dissolution of nifedipine solid dispersions with combined carriers. Chem. Pharm. Bull. 46, 482–487.

Tanno, F., Nishiyama, Y., Kokubo, H., Obara, S., 2004. Evaluation of hypromellose acetate succinate (HPMCAS) as a carrier in solid dispersions. Drug Dev. Ind. Pharm. 30, 9–17.

Tao, J., Sun, Y., Zhang, G.G., Yu, L., 2009. Solubility of small-molecule crystals in polymers: D-mannitol in PVP, indomethacin in PVP/VA, and nifedipine in PVP/VA. Pharm. Res. 26, 855–864.

Telang, C., Mujumdar, S., Mathew, M., 2009. Improved physical stability of amorphous state through acid base interactions. J. Pharm. Sci. 98, 2149–2159.

Vippagunta, S.R., Maul, K.A., Tallavajhala, S., Grant, D.J.W., 2002. Solid-state characterization of nifedipine solid dispersions. Int. J. Pharm. 236, 111–123.

Wang, L., Cui, F.D., Hayase, T., Sunada, H., 2005. Preparation and evaluation of solid dispersion for nitrendipine–carbopol and nitrendipine–HPMCP systems using a twin screw extruder. Chem. Pharm. Bull. 53, 1240–1245.

Wang, L., Cui, F.D., Sunada, H., 2007. Improvement of the dissolution rate of nitrendipine using a new pulse combustion drying method. Chem. Pharm. Bull. 55, 1119–1125.

Feasibility of ^{19}F-NMR for Assessing the Molecular Mobility of Flufenamic Acid in Solid Dispersions

Yukio Aso,* Sumie Yoshioka, Tamaki Miyazaki, and Toru Kawanishi

National Institute of Health Sciences; 1–18–1 Kamiyoga, Setagaya, Tokyo 158–8501, Japan.
Received September 9, 2008; accepted October 22, 2008; published online October 23, 2008

The purpose of the present study was to clarify the feasibility of ^{19}F-NMR for assessing the molecular mobility of flufenamic acid (FLF) in solid dispersions. Amorphous solid dispersions of FLF containing poly(vinylpyrrolidone) (PVP) or hydroxypropylmethylcellulose (HPMC) were prepared by melting and rapid cooling. Spin–lattice relaxation times (T_1 and $T_{1\rho}$) of FLF fluorine atoms in the solid dispersions were determined at various temperatures (−20 to 150 °C). Correlation time (τ_c), which is a measure of rotational molecular mobility, was calculated from the observed T_1 or $T_{1\rho}$ value and that of the T_1 or $T_{1\rho}$ minimum, assuming that the relaxation mechanism of spin–lattice relaxation of FLF fluorine atoms does not change with temperature. The τ_c value for solid dispersions containing 20% PVP was 2—3 times longer than that for solid dispersions containing 20% HPMC at 50 °C, indicating that the molecular mobility of FLF in solid dispersions containing 20% PVP was lower than that in solid dispersions containing 20% HPMC. The amount of amorphous FLF remaining in the solid dispersions stored at 60 °C was successfully estimated by analyzing the solid echo signals of FLF fluorine atoms, and it was possible to follow the overall crystallization of amorphous FLF in the solid dispersions. The solid dispersion containing 20% PVP was more stable than that containing 20% HPMC. The difference in stability between solid dispersions containing PVP and HPMC is considered due to the difference in molecular mobility as determined by τ_c. The molecular mobility determined by ^{19}F-NMR seems to be a useful measure for assessing the stability of drugs containing fluorine atoms in amorphous solid dispersions.

Key words ^{19}F-NMR; molecular mobility; stability; crystallization; solid dispersion

Amorphous solid dispersions are used for improving the dissolution rate and solubility of poorly soluble drugs. However, drugs in amorphous form are generally less stable than crystalline drugs because of their higher energy state and higher molecular mobility. It is well known that polymeric excipients can reduce the crystallization rate of many amorphous drugs.[1—12] This stabilization by poly(vinylpyrrolidone) (PVP) is partly attributable to its ability to decrease molecular mobility, as indicated by increases in the glass transition temperature (T_g).[9] Therefore, it is of great interest to estimate the molecular mobility of drugs in solid dispersions. Although ^{13}C-NMR relaxation measurements are useful for assessing the molecular mobility of drugs in solid dispersions,[13] the low sensitivity of ^{13}C because of its low natural abundance is a drawback of ^{13}C-NMR. In contrast to ^{13}C, ^{19}F has very favorable sensitivity in NMR experiments, since it is present in 100% natural abundance, is second only to the proton in its resonance frequency (except ^{3}H) and has a spin quantum number of 1/2. The receptivity for ^{19}F is 83% of that for ^{1}H and 4700 times of that for ^{13}C.[14] Many drugs containing fluorine atoms are listed in The Japanese Pharmacopoeia. In contrast, almost all pharmaceutical excipients do not contain fluorine atoms. ^{19}F-NMR may therefore have an advantage over ^{13}C-NMR or ^{1}H-NMR for selectivity and sensitivity when assessing the molecular mobility of drugs containing fluorine atoms in pharmaceutical dosage forms such as solid dispersions.

The orientations and molecular mobility of flufenamic acid (FLF)[15] and ^{19}F-labeled α-tocopherol[16] in a lipid bilayer were studied using ^{19}F-NMR. Structures and molecular mobility of ^{19}F-labeled peptides and proteins in biological membranes were also investigated.[17—20] To the authors' knowledge, application of ^{19}F-NMR to studies of drug molecular mobility in solid dispersions has not been reported. This paper describes the feasibility of ^{19}F-NMR for assessing the molecular mobility of FLF in PVP or hydroxypropylmethylcellulose (HPMC) solid dispersions, and discusses the effect of polymer excipients on the crystallization tendency of FLF in solid dispersions in terms of differences in molecular mobility.

Experimental

Materials FLF (Fig. 1) was purchased from Wako Pure Chemical Industry (Osaka), and PVP and HPMC were from Sigma (St. Louis, MO, U.S.A.). FLF solid dispersions with PVP or HPMC were prepared by melting and cooling of mixtures of FLF with PVP or HPMC. The solid dispersions obtained were confirmed to be amorphous from microscopic observation under polarized light.

Nuclear Magnetic Relaxation Measurements ^{19}F-NMR measurements were carried out using a model JNM-MU25 pulsed NMR spectrometer (JEOL DATUM, Tokyo) operating at a resonance frequency of 25 MHz. Time profiles of spin–spin relaxation of the ^{19}F atoms of FLF were measured using the "solid echo" pulse sequence to overcome the dead time of the instrument. Spin–lattice relaxation time in the laboratory frame (T_1) was measured using the inversion recovery pulse sequence. Spin–lattice relaxation time in the rotating flame ($T_{1\rho}$) was measured at spin locking intensity of 10 G.

DSC Measurements T_g of FLF-PVP and FLF-HPMC solid dispersions was measured by DSC using a model 2920 differential scanning calorimeter and a refrigerator cooling system (TA Instruments, Newcastle, DE, U.S.A.). Approximately 5 mg of each solid dispersions was put into an aluminum sample pan and then sealed hermetically. T_g was measured at a heating rate of 20 °C/min. Temperature calibration of the instrument was carried out using indium.

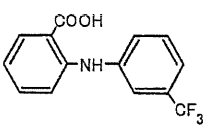

Fig. 1. Structure of FLF

* To whom correspondence should be addressed. e-mail: aso@nihs.go.jp

Results and Discussion

Molecular Mobility of FLF as Measured by ^{19}F-NMR Spin–Lattice Relaxation Time T_1 and $T_{1\rho}$ of fluorine atoms of FLF in PVP and HPMC solid dispersions were measured using a pulsed NMR spectrometer in the temperature range from −20 to 150 °C. T_1 is sensitive to the molecular motion on the time scale of the resonance frequency (MHz order). On the other hand, $T_{1\rho}$ is sensitive to the molecular motion with a frequency equivalent to the intensity of spin locking field (typically mid kHz order).[21] The temperature dependence of T_1 and $T_{1\rho}$ exhibits minimum at a specific temperature at which the molecules of interest have molecular motion with MHz time scale or mid kHz time scale predominantly. The resonance frequency of 25 MHz, lower than that of a conventional high resolution NMR spectrometer, was used to observe T_1 minimum in the temperature rage studied. Figure 2 shows the temperature dependence of T_1 and $T_{1\rho}$ of FLF fluorine atoms in PVP and HPMC solid dispersions. For FLF–PVP solid dispersions (7 : 3), the minimum of T_1 or $T_{1\rho}$ was observed at about 90 °C and 60 °C, respectively (Fig. 2A). When the PVP content decreased to 20% (w/w), T_1 and $T_{1\rho}$ of FLF at temperatures above 70 °C could not be determined due to rapid crystallization. Similar temperature dependence of T_1 or $T_{1\rho}$ was observed for the FLF–HPMC solid dispersions (Fig. 2B). The temperature difference between T_1 and $T_{1\rho}$ minimum is considered to be due to the difference in the time scale of molecular motion reflected on T_1 (MHz order) and $T_{1\rho}$ (mid kHz order). Since the molecular motion on MHz time scale becomes predominant at higher temperature than molecular motion on mid kHz time scale, T_1 minimum is observed at higher temperature than $T_{1\rho}$ minimum.

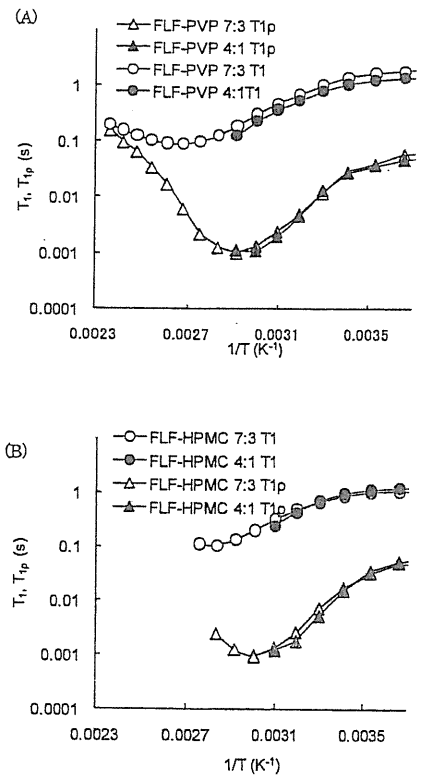

Fig. 2. Temperature Dependence of T_1 and $T_{1\rho}$ of FLF Fluorine Atoms in PVP (A) and HPMC (B) Solid Dispersions

We made following assumptions in order to estimate the molecular mobility of FLF from T_1 and $T_{1\rho}$ of FLF fluorine atoms: first, we assumed that FLF fluorine atoms in the solid dispersions relaxes mainly *via* dipolar interaction, and that the contribution of the spin–rotation interaction mechanism[21] is negligible. While relaxation *via* the spin–rotation interaction mechanism has been reported for liquid sample,[22–24] complete domination of dipolar interactions has been reported for fluorine atoms for polycrystalline van der Waals molecular solid.[25] We also made an assumption that the contribution of the cross-relaxation between fluorine and proton atoms can be considered small. It is known that relaxation is not intrinsically single-exponential when cross-relaxation between fluorine and proton atoms takes place.[14] However, we assumed small contribution of the cross-relaxation, because the relaxation of FLF fluorine atoms in the solid dispersions was exponential within experimental uncertainty. In studies of molecular motions, a large number of models describing molecular motions have been proposed for calculation of the spectrum density function.[26] We used a simple model that the molecular motion reflected on T_1 or $T_{1\rho}$ is represented by single correlation time for the purpose of comparing the mobility of FLF in the PVP and HPMC solid dispersions. According to the above assumptions, T_1 and $T_{1\rho}$ are described by Eqs. 1 and 2.[21]

$$\frac{1}{T_1} = \frac{6}{20}\frac{\gamma^4\hbar^2}{r^6}\left\{\frac{\tau_c}{1+\omega_0^2\tau_c^2} + \frac{4\tau_c}{1+4\omega_0^2\tau_c^2}\right\} \quad (1)$$

$$\frac{1}{T_{1\rho}} = \frac{3}{20}\frac{\gamma^4\hbar^2}{r^6}\left\{\frac{3\tau_c}{1+4\omega_1^2\tau_c^2} + \frac{5\tau_c}{1+\omega_0^2\tau_c^2} + \frac{2\tau_c}{1+4\omega_0^2\tau_c^2}\right\} \quad (2)$$

where τ_c is the correlation time that characterizes molecular reorientations, and ω_0 and ω_1 are the resonance frequencies of fluorine atoms in the static magnetic field and spin locking field, respectively. γ, r and $\hbar$ are the gyromagnetic ratio of fluorine, the distance of neighboring fluorine atoms, and the Plank constant divided by 2π, respectively. Equations 1 and 2 infer that T_1 and $T_{1\rho}$ become minimal when $\omega_0\tau_c$ is approximately 0.62[27] and $\omega_1\tau_c$ is approximately 0.52,[21] respectively. When the minimum of T_1 or $T_{1\rho}$ is observed, we can calculate the unknown value, r, in Eqs. 1 and 2. If r is known, the τ_c value can be calculated from the observed T_1 or $T_{1\rho}$ value, assuming that r does not change with temperature.

The values of r calculated from the T_1 and $T_{1\rho}$ minimum observed for the FLF–PVP solid dispersion (7 : 3) were 2.3 and 2.4 Å, respectively, and similar r values were obtained for the FLF–HPMC solid dispersion (7 : 3). These values are comparable to the reported value (2.174 Å) for 3-(trifluoromethyl)phenanthrene,[25] indicating that dipole interaction between neighboring fluorine atoms can be considered the predominant relaxation mechanism of FLF fluorine atoms in the solid dispersions. The difference between the r values obtained in this work and the reported value suggests that the possibility of the spin–rotation interaction mechanism and/or dipole interaction between fluorine and proton atoms cannot be excluded as a relaxation mechanism of FLF fluorine atoms.

Figure 3 shows the temperature dependence of τ_c calculated from T_1 and $T_{1\rho}$ for FLF fluorine atoms in the solid dis-

persions. The τ_c of FLF fluorine atoms in PVP solid dispersions calculated from $T_{1\rho}$ was 8.2 μs at 50 °C, which was about 3 times larger than that in HPMC solid dispersions (2.6 μs), indicating that the molecular mobility of FLF was lowered more strongly by PVP than by HPMC.

The τ_c values calculated using T_1 values differ from those calculated from $T_{1\rho}$ values. The slope of temperature dependence of τ_c changed around T_g. These findings suggest that the assumption that the molecular motion reflected on T_1 and $T_{1\rho}$ is represented by a single τ_c may be too simple to describe the molecular motion of FLF in the solid dispersions at temperatures studied, and that two or more molecular motions, such as rotation of trifluoromethyl group and motions with larger scales than rotation of trifluoromethyl group, may be reflected on T_1 and $T_{1\rho}$. Further studies including ^{1}H-NMR relaxation measurement and dielectric relaxation measurements will be needed to identify the detailed molecular motion of FLF in the solid dispersions.

Correlation between Crystallization Tendency and Molecular Mobility of FLF in Solid Dispersions Crystallization proceeds *via* formation of crystal nuclei and crystal growth. As a measure of the crystallization tendency of amorphous FLF in solid dispersions, the overall crystallization rate of amorphous FLF in the solid dispersions was estimated from the time profiles amorphous FLF remaining in the solid dispersions instead of measuring the nucleation rate and growth rate. Amorphous FLF remaining in the solid dispersions was estimated by analyzing solid echo signals of FLF fluorine atoms. Figure 4 shows the solid echo signal of fluorine atoms of FLF in solid dispersions containing 20% (w/w) PVP and that of fluorine atoms of crystalline FLF. The signal for the solid dispersions was describable by the Lorentzian relaxation equation (Eq. 3), and its relaxation time (T_{2L}) was approximately 140 μs. Crystalline FLF exhibited Gaussian relaxation signals (Eq. 4), and its relaxation time (T_{2G}) was approximately 30 μs. These results indicate that amorphous FLF in solid dispersions is considered to exhibit Lorentzian relaxation signals.

$$I=I_0 \exp(-t/T_{2L}) \tag{3}$$

$$I=I_0 \exp\{-t^2/(2T_{2G}^2)\} \tag{4}$$

where I_0 and I represent the signal intensities at time 0 and t, respectively. Figure 5 shows solid echo signals for the fluorine atoms of FLF in the solid dispersions stored at 60 °C. Samples stored at 60 °C exhibited biphasic decay signals, and signals were describable by summation of the Gaussian (solid line) and Lorentzian (dashed line) equations (Eq. 5).

$$I=I_0\{P_L \exp(-t/T_{2L})+P_G \exp(-t^2/2T_{2G}^2)\} \tag{5}$$

where P_L and P_G are the ratio of fluorine atoms exhibiting Lorentzian and Gaussian relaxation process, respectively, and $P_L+P_G=1$. Assuming that the T_{2L} and T_{2G} values are 140 and 30 μs, respectively, P_L values of FLF in the solid dispersions were estimated by curve fitting. P_L values of the solid dispersions decreased with increasing storage time, indicating that crystallization of amorphous FLF in solid dispersions takes place during storage at 60 °C. To certify the reliability of the P_L values obtained by ^{19}F-NMR measurements, change in the heat capacity at T_g ($\Delta C_p(T_g)$) was determined for the solid dispersions stored at 60 °C for various periods as a measure of amorphous FLF remaining, and was compared with the value of P_L. As shown in Fig. 6, the P_L value was proportional to the $\Delta C_p(T_g)$ value, and was considered to be a useful measure of amorphous FLF remaining in the solid dispersions.

Figure 7 shows the time profiles of the P_L values for FLF solid dispersions containing 20% (w/w) PVP or HPMC at 60 °C. The decrease in the ratio of Lorentzian fluorine atoms was faster for HPMC solid dispersions than for PVP solid dispersions, indicating that the overall crystallization rate of FLF in HPMC solid dispersions is larger than that in PVP solid dispersions. The overall crystallization rate depends on both molecular mobility (the rate of diffusion across the interface between crystalline and amorphous phase) and ther-

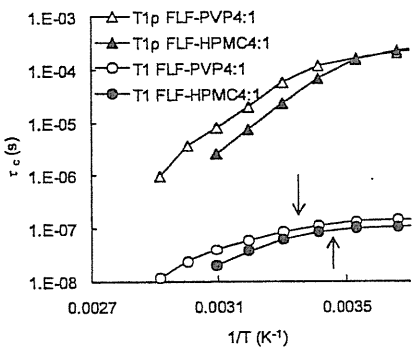

Fig. 3. Temperature Dependence of τ_c of FLF Fluorine Atoms in PVP and HPMC Solid Dispersions

Arrows in the figure represent T_g.

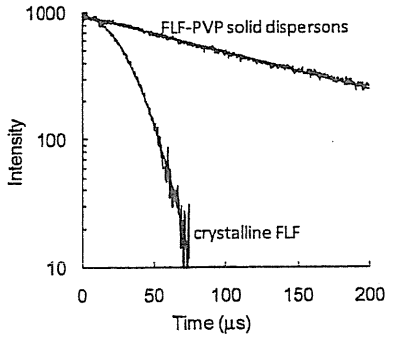

Fig. 4. Typical Solid Echo Signal of Fluorine Atoms of FLF in the Freshly Prepared Solid Dispersion Containing 20% (w/w) PVP and That of Fluorine Atoms of Crystalline FLF

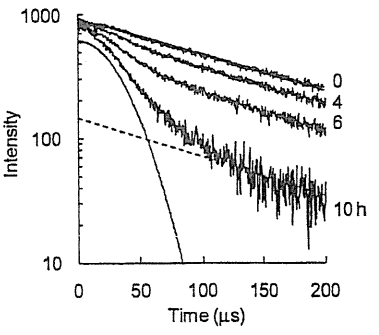

Fig. 5. Typical Solid Echo Signals of Fluorine Atoms of FLF in the Solid Dispersions Containing 20% (w/w) PVP Stored at 60 °C

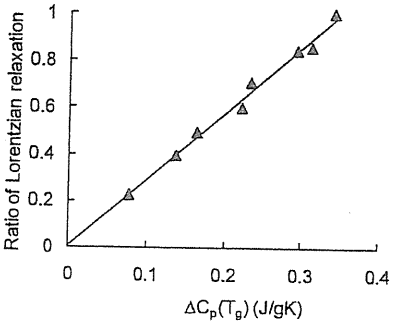

Fig. 6. The Ratio of FLF Fluorine Atoms Exhibiting Lorentzian Relaxation as a Function of Changes in the Heat Capacity at T_g

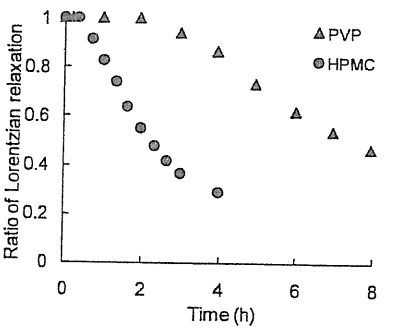

Fig. 7. Time Profiles of the Ratio of FLF Fluorine Atoms Exhibiting Lorentzian Relaxation in PVP and HPMC Solid Dispersions Stored at 60 °C

modynamic factors, such as free energy difference between crystalline and amorphous form.[2,3,10] Differences in the overall crystallization rate of amorphous FLF are consistent with those in the molecular mobility (Fig. 3), suggesting that the molecular mobility as determined by the ^{19}F-NMR spin–lattice relaxation times may be one of the factors determining crystallization rate, and useful as a measure of the physical stability of FLF in solid dispersions. The T_g values of the solid dispersions containing 20% PVP and 20% HPMC were 23 °C and 15 °C, respectively, indicating that molecular mobility reflected on T_g is higher for the solid dispersion containing HPMC than for that containing PVP. The T_g data seem to support the speculation obtained from NMR data. However, the scale of molecular mobility reflected on T_g is considered to be larger than that reflected on τ_c. Further studies should be conducted to elucidate the quantitative correlation between the physical stability of amorphous FLF and the molecular mobility determined by ^{19}F-NMR.

In conclusion, ^{19}F-NMR is useful for elucidating the molecular mobility of drugs containing fluorine atoms in amorphous solid dispersions. τ_c values of FLF fluorine atoms were calculated from the ^{19}F-NMR spin–lattice relaxation data. The τ_c value for solid dispersions containing 20% PVP was 2—3 times longer than that for solid dispersions containing 20% HPMC at 50 °C. Molecular mobility of FLF in the solid dispersions containing 20% PVP was lower than in those containing 20% HPMC, and this was consistent with the fact that the overall crystallization rate of amorphous FLF in the solid dispersion containing PVP was smaller than in that containing HPMC. The molecular mobility determined by ^{19}F-NMR seems to be useful as a measure of the physical stability of an amorphous drug in solid dispersions.

Acknowledgements Part of this work was supported by a Grant-in-aid for Research on Publicly Essential Drugs and Medical Devices from The Japan Health Sciences Foundation.

References

1) Yoshioka M., Hancock B. C., Zografi G., *J. Pharm. Sci.*, **84**, 983—986 (1995).
2) Matsumoto T., Zografi G., *Pharm. Res.*, **16**, 1722—1728 (1999).
3) Crowley K. J., Zografi G., *Pharm. Res.*, **20**, 1417—1422 (2003).
4) Shamblin S. L., Huang E. Y., Zografi G., *J. Therm. Anal.*, **47**, 1567—1579 (1996).
5) Shamblin S. L., Zografi G., *Pharm. Res.*, **16**, 1119—1124 (1999).
6) Zeng X. M., Martin G. P., Marriott C., *Int. J. Pharm.*, **218**, 63—73 (2001).
7) Miyazaki T., Yoshioka S., Aso Y., Kojima S., *J. Pharm. Sci.*, **93**, 2710—2717 (2004).
8) Khougaz K., Clas S., *J. Pharm. Sci.*, **89**, 1325—1334 (2000).
9) Berggren J., Alderborn G., *Eur. J. Pharm. Sci.*, **21**, 209—215 (2004).
10) Aso Y., Yoshioka S., Kojima S., *J. Pharm. Sci.*, **93**, 384—391 (2004).
11) Miyazaki T., Yoshioka S., Aso Y., *Chem. Pharm. Bull.*, **54**, 1207—1210 (2006).
12) Konno H., Taylor L. S., *J. Pharm. Sci.*, **95**, 2692—2705 (2006).
13) Aso Y., Yoshioka S., *J. Pharm. Sci.*, **95**, 318—325 (2006).
14) Harris R. K., Monti G. A., Holstein P., "Solid State NMR of Polymers," Chap. 6, ed. by Ando I., Asakura T., Elsevier, Amsterdam, 1998, pp. 351—414.
15) Grage S. L., Ulrich A. S., *J. Magn. Reson.*, **146**, 81—88 (2000).
16) Urano S., Matsuo M., Sakanaka T., Uemura I., Koyama M., Kumadaki I., Fukuzawa K., *Arch. Biochem. Biophys.*, **303**, 10—14 (1993).
17) Afonin S., Glaser R. W., Berditchevskaia M., Wadhwani P., Gührs K. H., Möllmann U., Perner A., Ulrich A. S., *ChemBioChem*, **4**, 1151—1163 (2003).
18) Salgado J., Grage S. L., Kondejewski L. H., Hodges R. S., McElhaney R. N., Ulrich A. S., *J. Biomol. NMR*, **21**, 191—208 (2001).
19) Williams S. P., Haggie P. M., Brindle K. M., *Biophys. J.*, **72**, 490—498 (1997).
20) Quint P., Ayala I., Busby S. A., Chalmers M. J., Griffin P. R., Rocca J., Nick H. S., Silverman D. N., *Biochemistry*, **45**, 8209—8215 (2006).
21) Farrar T. C., Brcker E. D., "Pulse and Fourier Transform NMR," Academic Press, New York and Lodon, 1971.
22) Namgoong H., Lee J. W., *Bull. Korean Chem. Soc.*, **14**, 91—95 (1993).
23) Huang S.-G., Rogers M. T., *J. Chem. Phys.*, **68**, 5601—5606 (1978).
24) Gutowsky H. S., Lawrenceson I. J., Shimomura K., *Phys. Rev. Lett.*, **6**, 349—351 (1961).
25) Beckmann P. A., Rosenberg J., Nordstrom K., Mallory C. W., Mallory F. B., *J. Phys. Chem. A*, **110**, 3947—3953 (2006).
26) Horii F., "Solid State NMR of Polymers," Chap. 3, ed. by Ando I., Asakura T., Elsevier, Amsterdam, 1998, pp. 51—82.
27) Ruan R. R., Chen P. L., "Water in Foods and Biological Materials," Chap. 7, Technomic Publishing Co., Lancaster Basel, 1998, pp. 253—278.

Importance of Neonatal FcR in Regulating the Serum Half-Life of Therapeutic Proteins Containing the Fc Domain of Human IgG1: A Comparative Study of the Affinity of Monoclonal Antibodies and Fc-Fusion Proteins to Human Neonatal FcR

Takuo Suzuki,* Akiko Ishii-Watabe,* Minoru Tada,* Tetsu Kobayashi,* Toshie Kanayasu-Toyoda,* Toru Kawanishi,† and Teruhide Yamaguchi*

The neonatal FcR (FcRn) binds to the Fc domain of IgG at acidic pH in the endosome and protects IgG from degradation, thereby contributing to the long serum half-life of IgG. To date, more than 20 mAb products and 5 Fc-fusion protein products have received marketing authorization approval in the United States, the European Union, or Japan. Many of these therapeutic proteins have the Fc domain of human IgG1; however, the serum half-lives differ in each protein. To elucidate the role of FcRn in the pharmacokinetics of Fc domain-containing therapeutic proteins, we evaluated the affinity of the clinically used human, humanized, chimeric, or mouse mAbs and Fc-fusion proteins to recombinant human FcRn by surface plasmon resonance analysis. The affinities of these therapeutic proteins to FcRn were found to be closely correlated with the serum half-lives reported from clinical studies, suggesting the important role of FcRn in regulating their serum half-lives. The relatively short serum half-life of Fc-fusion proteins was thought to arise from the low affinity to FcRn. The existence of some mAbs having high affinity to FcRn and a short serum half-life, however, suggested the involvement of other critical factor(s) in determining the serum half-life of such Abs. We further investigated the reason for the relatively low affinity of Fc-fusion proteins to FcRn and suggested the possibility that the receptor domain of Fc-fusion protein influences the structural environment of the FcRn binding region but not of the FcγRI binding region of the Fc domain. *The Journal of Immunology*, **2010, 184: 1968–1976.**

In healthy humans, IgG1 exhibits a long serum half-life of ~21 d (1). This prolonged half-life of IgG can be explained by the interaction with neonatal FcR (FcRn). FcRn is a heterodimer of the MHC class I-like H chain and the β_2-microglobulin (β_2m) L chain (2). Although this receptor was originally studied as a transporter of IgG from mother to fetus, subsequent studies have shown that this receptor also plays a critical role in regulating IgG homeostasis (3, 4). FcRn binds to the Fc domain of IgG at pH 6.0–6.5 but not, or weakly, at pH 7.0–7.5 (5). Therefore, FcRn protects IgG from degradation by binding to IgG in endosome and releases IgG into plasma (6). As indicated by previous studies in which amino acid substitutions in the Fc domain of IgG for modifying the affinity to FcRn can alter the serum half-life of the IgG, the affinity to FcRn is thought to play a critical role in determining the serum half-life of IgG (7–12).

Recently, therapeutic use of mAb products has become more important for various diseases, including cancer as well as autoimmune and infectious diseases (6, 13, 14). In addition to the mAbs, the Fc-fusion proteins (e.g., etanercept, alefacept, and abatacept) have been developed and have received considerable attention. These Fc-fusion proteins consist of an extracellular domain of membrane receptor linked to the Fc portion of human IgG1. They work like Abs by binding to ligands for the receptors. The receptor portions of etanercept and alefacept are, respectively, the extracellular ligand-binding portion of the human 75-kDa TNFR and the extracellular CD2-binding portion of the human leukocyte function Ag 3. Abatacept consists of the extracellular domain of human CTLA-4 linked to the modified Fc portion of human IgG1.

Most of the mAb products and Fc-fusion protein products have the Fc domain of human IgG1 (6, 14). Accumulating evidence regarding their clinical use has revealed that their serum half-lives are variable, ranging from 4 to 23 d, regardless of the presence of the Fc domain of human IgG1 (6). Although many factors such as m.w., posttranslational modifications including glycosylation, electrical properties, interactions with FcRs or target molecules, and features of the target molecules may influence their serum half-life, the reasons for the variability of half-life have not been elucidated. Among such factors, FcRn might play a critical role in regulating half-life; however, comparative studies between the affinities of these therapeutic proteins to FcRn and their half-lives in humans have not been reported. Therefore, although some Fc domain-containing therapeutic proteins exhibit shorter half-lives in humans, it remains unclear whether the shorter half-lives are due to the lower affinity to FcRn or other factors.

*Division of Biological Chemistry and Biologicals and †Division of Drugs, National Institute of Health Sciences, Tokyo, Japan

Received for publication October 8, 2009. Accepted for publication December 16, 2009.

This work was supported in part by Grant-in-Aid for Young Scientists 21790172 from the Ministry of Education, Culture, Sports, Science, and Technology, and Grants-in-Aid for Scientific Research 18590163 and 20590167 from Japan Society for the Promotion of Science.

Address correspondence and reprint requests to Dr. Akiko Ishii-Watabe, National Institute of Health Sciences, 1-18-1 Kamiyoga, Setagaya-ku, Tokyo 158-8501, Japan. E-mail address: watabe@nihs.go.jp

Abbreviations used in this paper: β_2m, β_2-microglobulin; FcRn, neonatal FcR; HER2, human epidermal growth factor receptor 2; ND, not detected; R^2, coefficient of determination; SPR, surface plasmon resonance.

www.jimmunol.org/cgi/doi/10.4049/jimmunol.0903296

In this study, we examined the affinity of clinically used mAbs and Fc-fusion proteins to recombinant human FcRn by surface plasmon resonance (SPR) analysis. The analytes used were human Ab (adalimumab), humanized Abs (daclizumab, omalizumab, palivizumab, and trastuzumab), chimeric Abs (infliximab and rituximab), mouse Ab (muromonab-CD3), and Fc-fusion proteins (etanercept, alefacept, and abatacept). We found that the affinities of the therapeutic proteins tested to FcRn were closely correlated with their serum half-lives, with a few exceptions. Because Fc-fusion proteins, which have relatively short half-lives (4–13 d), were shown to have lower affinity to FcRn than mAbs, we further investigated the reason for this difference by examining the affinity of the proteins to FcγRI or the affinity of papain-digested proteins to FcRn in SPR analyses. Our results suggested the possibility that the receptor portions of Fc-fusion proteins make a difference in the higher-order structure of the FcRn-binding region of Fc (i.e., CH2-CH3 interface) or interfere with binding between the Fc domain and FcRn by steric hindrance.

Materials and Methods

Therapeutic proteins and reagents

Abatacept (Bristol-Myers Squibb, Princeton, NJ), adalimumab (Abbott, Baar, Switzerland), alefacept (Biogen Idec, Cambridge, MA), daclizumab (Hoffmann-La Roshe, Nutley, NJ), etanercept (Takeda Pharmaceutical, Osaka, Japan), infliximab (Tanabe Phamaceutical, Osaka, Japan), muromonab-CD-3 (Jansen Pharmaceutical, Tokyo, Japan), omalizumab (Novartis Pharma Schweiz, Bern, Switzerland), palivizumab (Abbott Japan, Osaka, Japan), rituximab (Zenyaku Kogyo, Tokyo, Japan), and trastuzumab (Chugai Pharmaceutical, Tokyo, Japan) were purchased via reagent distributors. Recombinant human TNF-α was purchased from Wako (Osaka, Japan).

Purification of human FcRn

Stably transfected CHO cells expressing both the soluble portion of the hFcRn H chain (residues 1–267 of mature protein) and β_2m were provided by P. J. Bjorkman (California Institute of Technology, Pasadena, CA). Expression and purification of hFcRn were performed according to the method previously reported by West and Bjorkman (15), with slight modifications. Briefly, the CHO cells expressing soluble hFcRn and β_2m were cultured in α-MEM containing 5% dialyzed FBS, 100 μM methionine sulfoximine, and penicillin/streptomycin. Cell culture supernatant was collected every 2–3 d and was filtered with a 0.45-μm filter, and sodium azide was then added to 0.05%. The harvested supernatant was acidified to pH 5.8 and then applied to a human IgG column. After washing the column with 50 mM Bis-Tris (pH 5.8), hFcRn complexed with β_2m was eluted with 40 mM Bis-Tris/20 mM Tris (pH 8.1). The eluted fractions containing hFcRn were applied to a Uno-Q1 column, and hFcRn was eluted with pH gradient using 40 mM Bis-Tris/20 mM Tris (pH 8.1) and 40 mM Bis-Tris/20 mM Tris (pH 5.8).

SDS-PAGE and Western blotting

Each fraction of protein eluted from the Uno-Q1column was diluted in 1× SDS loading buffer and was separated in 15% polyacrylamide gel (Bio craft, Tokyo, Japan). After the electrophoresis, the gels were stained with Imperial protein stain (Pierce, Rockford, IL). For Western blotting, proteins separated by SDS-PAGE were electroblotted onto polyvinylidene difluoride membranes (Millipore, Billerica, MA). The membranes were immunoreacted with rabbit anti-hFcRn H chain peptide (Leu^{135}-Gly^{148}) Ab produced by Medical and Biological Laboratories (Nagoya, Japan) and then with HRP-conjugated secondary Abs (Cell Signaling Technology, Danvers, MA). The bands of hFcRn were detected using ECL Plus Western blotting detection reagents (Amersham Biosciences, Piscataway, NJ).

SPR analyses

Analysis of affinity between FcRn and Fc domain-containing therapeutic proteins. The purified recombinant hFcRn was diluted with 10 mM sodium acetate (pH 5.0 or 4.5) and was immobilized onto a CM5 biosensor chip (Biacore, Uppsala, Sweden) using an amine coupling kit (Biacore) at relatively low densities (mainly 300–350 resonance units) to avoid mass transport limitation. The reference cell was treated with *N*-hydroxysuccinimide/1-ethyl-3-(3-dimethylaminopropyl) carbodiimide and ethanol amine using an amine coupling kit without injecting the FcRn. Fc domain-containing proteins were diluted with the running buffer (50 mM sodium phosphate/150 mM NaCl [pH 6.0]) and injected at 25°C. The running buffer was allowed to flow at a rate of 20 μl/min. The injections were performed using the KINJECT mode (volume, 40 μl; dissociation time, 150 s). For regeneration, the regeneration buffer (100 mM Tris/200 mM NaCl [pH 8.0]) was injected for 4 min. Kinetic constants were calculated from the sensorgrams using the bivalent analyte model of BIAevaluation software 4.1.

To obtain the consistent results, we would indicate two points. First, it is necessary to set the bulk refractive index to zero to avoid wrong fitting, because the binding is rapidly reached to the near-equilibrium state. Second, it is necessary to set the injection point correctly. For example, if the sensorgrams of infliximab shown in Fig. 2 were analyzed with the injection point shifted to 0.5 s earlier, the values of k_{a1}, k_{d1}, and K_D were 1.95E+05 $M^{-1}s^{-1}$, 0.136 s^{-1}, and 697 nM, respectively. When the injection points of the sensorgrams are unclear, it may be better to use the average values of data resulting from two or more different injection points.

Analysis of affinity between FcγRI and Fc domain-containing therapeutic proteins. Recombinant human FcγRI, which consists of human FcγRI (Gln^{16}-Pro^{288}) and His-tag, was purchased from R&D Systems (Minneapolis, MN). Fc domain-containing proteins were immobilized to a CM5 biosensor chip in 10 mM sodium acetate (pH 5.0) using an amine coupling kit. Kinetic analyses of FcγRI binding were performed according to Ellsworth et al. (16) with some modifications. The running buffer, HBS-EP (10 mM HEPES, 150 mM NaCl, 3 mM EDTA, and 0.005% Surfactant P20 [pH 7.4]) (Biacore), was allowed to flow at 20 μl/min. The injections of FcγRI were performed using the KINJECT mode (volume, 40 μl; dissociation time, 150 s). To regenerate the immobilized proteins, the regeneration buffer (10 mM glycine-HCl [pH 1.8]) was injected for 15 s. Kinetic constants were derived from the sensorgrams using the 1:1 binding model of BIAevaluation software 4.1.

Papain digestion

The papain (Wako) was activated in the buffer (50 mM sodium phosphate/150 mM NaCl [pH 6.0], 1 mM cysteine, 4 mM EDTA, and 1 mg/ml papain) at 37°C for 15 min. Next, 1 mg/ml Ab or Fc-fusion protein was digested with 0.1 mg/ml activated papain in 50 mM sodium phosphate (pH 6.0), 150 mM NaCl, 0.1 mM cysteine, and 4 mM EDTA at 37°C for 24 h.

Results

Purification of soluble human FcRn

FcRn binds to the Fc domain at acidic pH and then releases it at neutral pH. Recombinant soluble hFcRn expressed from CHO cells was purified using a human IgG column by binding at pH 5.8 and releasing at pH 8.1. The fraction purified by the IgG column was electrophoresed at lane 10 of SDS-PAGE gel (Fig. 1*B*). This fraction was then purified using an anion-exchange column with a pH gradient elution. The elution diagram is shown in Fig. 1*A*. Three main peaks were observed. The proteins in these peaks were electrophoresed (Fig. 1*B*) and subjected to Western blot analysis using anti-hFcRn H chain peptide Ab (Fig. 1*C*). Several bands were observed at ~32 kDa in these fractions, and these bands were immunoreactive to anti-hFcRn H chain peptide Ab. These results indicated that the purified FcRn had several isoforms, possibly because of the difference in posttranslational modification, including glycosylation or proteolysis. As shown in Fig. 1*C*, the signals of the higher m.w. bands of hFcRn tend to be weak. There is a possibility that the sugar chain at Asn^{125} of hFcRn interfered with the reactivity of the hFcRn to the anti-hFcRn H chain peptide Ab used. We analyzed the affinity of therapeutic mAbs and Fc fusion proteins to FcRn by SPR using the peak I, II, or III fractions eluted from the anion-exchange column. The K_D values were higher when peak I was used as a ligand in SPR analyses than when peaks II or III were used (data not shown). Because the m.w. of the proteins in peak I was smaller than that in peak II/III and the protein content of peak I varied depending on the lot of the cell culture supernatant, peak I seemed to consist of immature FcRn. The K_D values calculated from the experimental data using peaks II and III were comparable (data not shown). We, therefore, used the main peak (i.e., peak III) in the following experiments.

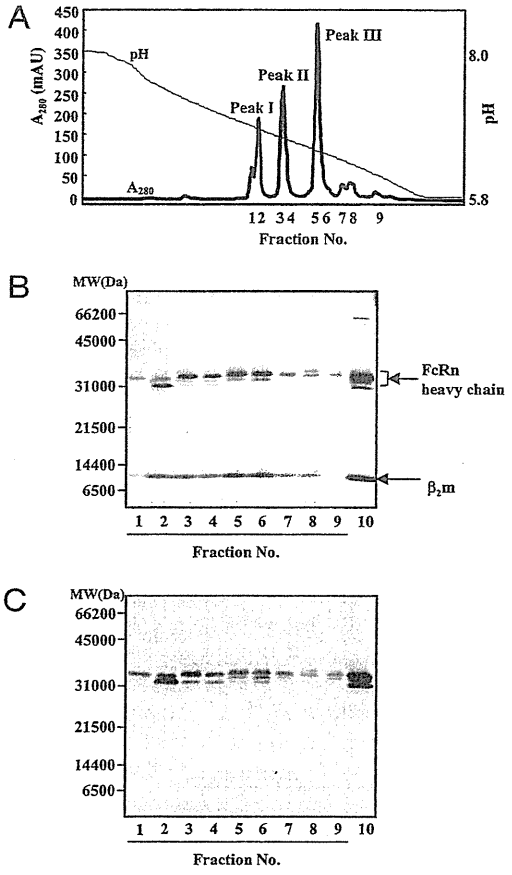

FIGURE 1. Purification and electrophoretic characterization of recombinant human FcRn. *A*, The elution diagram of the anion-exchange chromatography used for the purification of recombinant human FcRn. *B*, SDS-PAGE of the proteins in the fractions indicated in *A*. The protein applied to the anion-exchange column was electrophoresed in *lane 10*. The gel was stained with Imperial protein stain. *C*, Western blot analysis of eluate from the anion-exchange column by anti-hFcRn H chain Ab.

SPR analyses of the affinity between FcRn and Fc domain-containing proteins

Purified FcRn was immobilized onto a CM5 biosensor chip at relatively low densities as described in *Materials and Methods*. Five or six concentrations of Fc domain-containing therapeutic proteins were then injected. Because injection at higher concentrations caused nonspecific binding to flow cells, we analyzed the affinity of therapeutic proteins using sensorgrams obtained at the concentrations at which nonspecific binding was not observed. For example, infliximab was injected at concentrations of 670, 335, 168, 84, and 42 nM, and we analyzed the affinity to FcRn with the bivalent analyte model (Fig. 2). The colored lines were observed sensorgrams, and the black lines were fitting lines generated by the BIAevaluation software. The K_D value ($= k_{d1}/k_{a1}$) calculated from these sensorgrams was 727 nM. The affinities of adalimumab and etanercept to FcRn were 672 and 3612 nM, respectively (Fig. 2).

The affinities of the 11 kinds of Fc domain-containing proteins to FcRn were measured (Fig. 3). Adalimumab, daclizumab, infliximab, palivizumab, and rituximab were injected at concentrations of 42–670 nM. The concentrations of abatacept, alefacept, and etanercept used were 168–5360 nM, and those of muromonab-CD3, omalizumab, and trastuzumab were 84–1340 nM. Under this condition, the tested therapeutic proteins, except for muromonab-CD3, bound to FcRn. The K_D values measured in our experiments and the serum half-lives in humans reported in the literature are shown in Fig. 3*A*.

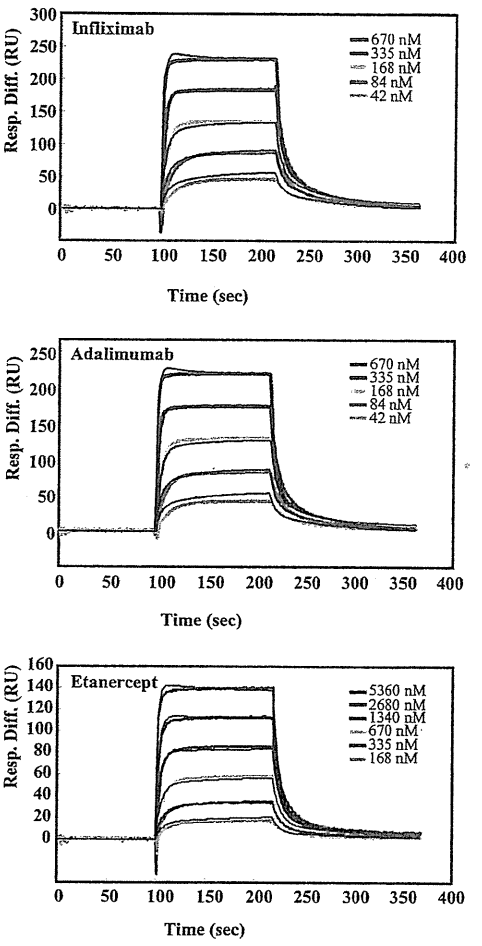

	Infliximab	Adalimumab	Etanercept
k_a1 (1/Ms)	2.09E+05	2.41E+05	3.71E+04
k_d1 (1/s)	0.152	0.162	0.134
k_a2 (1/RUs)	4.56E-05	3.98E-05	3.27E-05
k_d2 (1/s)	9.78E-03	8.80E-03	5.44E-03
Rmax (RU)	3.76E+02	3.47E+02	1.93E+02
Chi2	1.80E+01	1.74E+01	5.37E+00
$K_D=k_d1/k_a1$	**727 nM**	**672 nM**	**3612 nM**

FIGURE 2. Representative sensorgrams of SPR analyses. Infliximab (*upper panel*) or adalimumab (*middle panel*) was injected at concentrations of 42–670 nM and etanercept (*lower panel*) at concentrations of 168–5360 nM. The colored lines are the observed sensorgrams, and the black lines are fitting lines generated by the bivalent analyte model of BIAevaluation software. The association of KINJECT was started at ~100 s, and the dissociation of KINJECT was at ~220 s. The table describes the kinetic values calculated from the sensorgrams of infliximab, adalimumab, and etanercept.

The K_D values and the average values of the serum half-lives are plotted in Fig. 3*B*. The K_D values were closely correlated to the half-lives (contribution ratio = 0.8675) when the results were analyzed after excluding the data for infliximab, rituximab, and trastuzumab (Fig. 3*C*). Concerning infliximab, rituximab, and trastuzumab, which have relatively short half-lives and comparable affinity to other long half-life Abs to FcRn, other critical factor(s) seemed to be involved in regulating their half-lives (see *Discussion*). Although it was impossible to plot the data for mouse mAb muromonab-CD3,

A

Structure	Nonproprietary name	Binding target	Affinity to FcRn K_D (nM)	Half-life (days) cited from the literature	
Human antibody	Adalimumab	TNFα	672	14.7-19.3	Weisman et al., 2003
Humanized antibody	Daclizumab	CD25	846	20	Vincenti et al., 1998
	Omalizumab	IgE	1237	20	Casale et al., 1997
	Palivizumab	RSV F protein	750	19-27	Subramanian et al., 1998
	Trastuzumab	HER2	773	2.7-10	Tokuda et al., 1999
Chimeric antibody	Infliximab	TNFα	727	9.5	Comillie et al., 2001
	Rituximab	CD20	508	9.4	Maloney et al., 1997
Mouse antibody	Muromonab-CD3	CD3	ND	0.75	Hooks et al., 1991
Fc-fusion protein	Abatacept	CD80/CD86	2633	13.1	prescribing information
	Alefacept	CD2	2506	11.3	prescribing information
	Etanercept	TNFα	3612	4	Lee et al., 2003

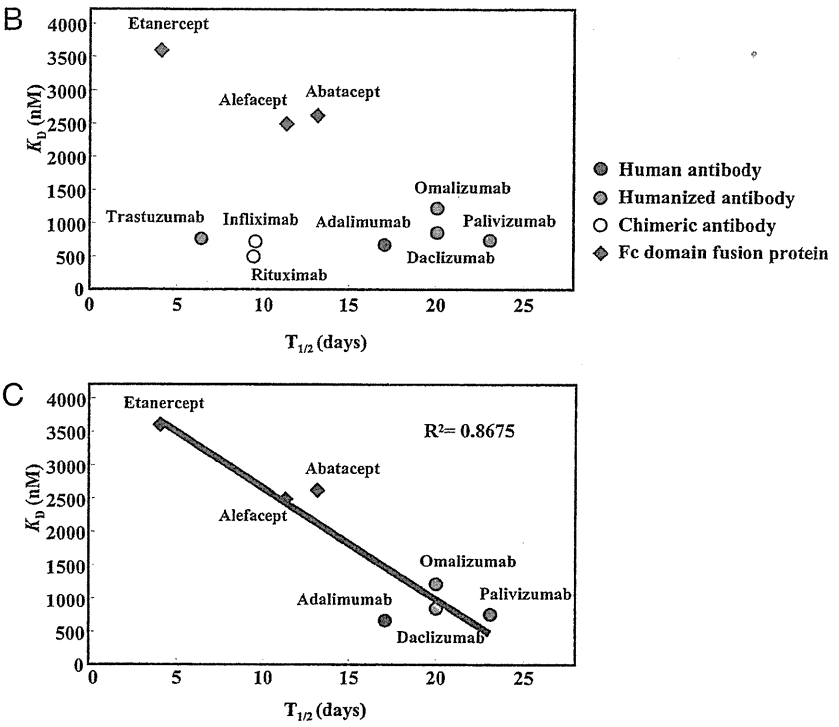

FIGURE 3. K_D values of binding between Fc domain-containing therapeutic proteins and hFcRn and the correlation with their serum half-lives. *A*, The K_D values obtained in our study and the half-lives in humans cited from the literature. The half-life values were obtained from the article reviewed by Lobo et al. (6) [adalimumab (17), daclizumab (18), etanercept (19), infliximab (20), muromonab-CD3 (21), omalizumab (22), palivizumab (23), rituximab (24), and trastuzumab (25)] or from the manufacturer prescribing information. *B*, The graphical presentation of the K_D values and serum half-lives described in *A*. The means of half-lives are plotted on the *x*-axis, and the values of affinity to FcRn are on the *y*-axis. Filled rhombi, Fc domain fusion proteins; closed circle, human Ab; gray circles, humanized Abs; open circle, chimeric Abs. *C*, Regression line of the plots of seven therapeutic proteins. ND, not detected; R^2, coefficient of determination.

which exhibited no significant binding to human FcRn, the half-life of this Ab in humans is the shortest (0.75 d) among the therapeutic proteins examined in this study (21). These results also show the importance of the binding affinity to FcRn in determining the serum half-life. The correlation described above was also observed when other fractions of hFcRn described in Fig. 1 (peaks I and II) were used in SPR analyses (data not shown).

The affinity between FcγRI and Fc domain-containing proteins

Because the affinities of Fc fusion proteins (etanercept, alefacept, and abatacept) to FcRn were lower than those of mAbs, the FcRn-binding region (CH2-CH3 domain interface) of Fc-fusion proteins seems to be structurally different from that of mAbs. We also analyzed the affinity of these proteins to FcγRI to test whether the structural environment around the FcγRI-binding region (hinge proximal region of CH2) is different between Fc-fusion proteins and Abs. Because the regeneration procedure in the SPR assay inactivated FcγRI but not Fc domain-containing therapeutic proteins, therapeutic proteins were immobilized to CM5 biosensor chips, and FcγRI was used as an analyte. The sensorgrams of Fc-fusion proteins (abatacept, alefacept, and etanercept) and mAbs (adalimumab and infliximab) are shown in Fig. 4*A*. The data were analyzed with a 1:1 binding model. The K_D values of the two Fc fusion proteins (alefacept and etanercept) and Abs (adalimumab and infliximab) were comparable (Fig. 4*B*). The K_D values obtained in this study were similar to the data reported for IgG [reviewed by van de Winkel and Anderson (26)]. In contrast, abatacept had a lower affinity to FcγRI. In abatacept, a series of selected mutations those can alter the binding affinity to FcγR were introduced to reduce Fc-mediated cytotoxic effects (Fig. 5) (28, 29). Therefore, the data in Fig. 4 show that the change in the affinity of Fc domain to FcγRI, which is caused by amino acid substitutions, was detected in our experiments. These results suggest that the region interacting with FcγRI (i.e., the hinge proximal region of CH2) was not structurally different between Fc fusion proteins, except for abatacept, and Abs examined.

The affinity between FcRn and Fc domains generated by papain treatment

In Fig. 5, the amino acids sequences of abatacept, alefacept, etanercept, adalimumab, infliximab, and omalizuamb are aligned. The differences in the primary structure of the Fc regions were Glu^{376} and Met^{378} of etanercept, which are attributed to the IgG1 allotype, and Ser^{162}, Ser^{165}, and Ser^{174} of abatacept, which are due

A

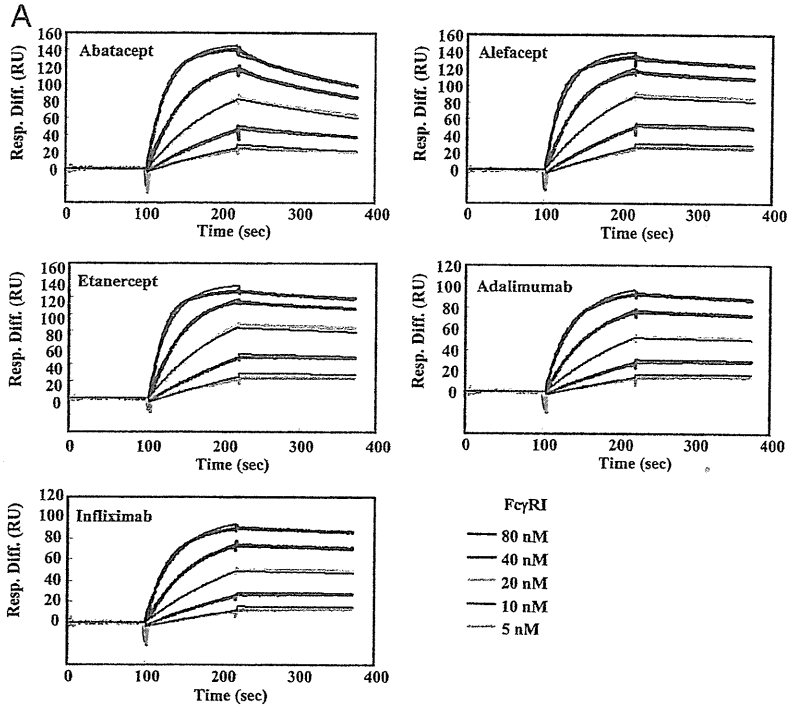

FIGURE 4. The affinity of Fc-fusion proteins and Abs to FcγRI. The Fc-fusion proteins (abatacept, alefacept, and etanercept) and mAbs (adalimumab and infliximab) were immobilized onto CM5 biosensor chips. Recombinant protein of the extracellular domain of FcγRI was injected at concentrations of 5–80 nM and analyzed with a 1:1 binding model (*A*). The colored lines are the observed sensorgrams, and the black lines are fitting lines. Association phase, ~100–220 s; dissociation phase, ~220 s. *B*, The K_D values calculated from the sensorgrams shown in *A*.

B

	Affinity to FcγRI K_D (nM)
Abatacept	4.82
Alefacept	0.857
Etanercept	0.818
Adalimumab	0.779
Infliximab	0.763

to the engineering for decreasing affinity to FcγR and improving protein production (28). To test the possibility that this limited structural difference or posttranscriptional modifications such as glycosylation can give rise to the difference in binding affinity to FcRn, we digested the Fc-fusion proteins or mAbs with papain and analyzed the affinity of their Fc domains to FcRn. The electrophoretic pattern of etanercept and adalimumab digested with papain is shown in Fig. 6*A*. Both etanercept and adalimumab were digested sufficiently for 24 h at 37°C under the conditions described in *Materials and Methods*, whereas digestion was not sufficient after incubating for 2 h. Therefore, the therapeutic proteins digested with papain for 24 h were used for the SPR analyses. The sensorgrams of etanercept (670 nM) and adalimumab (670 nM) were much different without incubation with papain, but they became almost identical after papain digestion (Fig. 6*B*). We measured the affinities to FcRn of five therapeutic proteins (etanercept, alefacept, adalimumab, infliximab, and omalizumab) digested with papain (Fig. 6*C*). Etanercept and alefacept are Fc-fusion proteins with low affinity to FcRn, and omalizumab is an Ab showing lower affinity to FcRn than other Abs. Because it was possible that the proteins were cleaved, in part, into smaller fragments than the Fc domain, the estimated K_D values may have been larger than the actual values. However, it was very clear that the affinities of etanercept, alefacept, infliximab, and omalizumab were increased by papain treatment (Fig. 6*C*).

The affinity of Fc-fusion protein and Abs became comparable after papain digestion, showing that the differences in amino acid sequences or posttranslational modification of the Fc domain did not contribute to the difference in the binding affinity of these proteins to FcRn. It therefore seems likely that the receptor domain of the Fc-fusion protein makes a difference in the higher-order structure of the FcRn-binding region of Fc (i.e., CH2-CH3 interface) or interferes with the binding between Fc domain and FcRn by steric hindrance. Moreover, such a difference or interference seems to be involved in determining the affinity to FcRn for some kinds of Abs, because the K_D values of infliximab and omalizumab were also increased significantly by papain treatment.

The affinity between FcRn and therapeutic proteins binding with target molecules

On the basis of the results suggesting the possibility that another region besides the Fc domain influences the affinity of Fc domain-containing proteins to FcRn, we assumed that binding with the target molecule would also change the affinity to FcRn. Because adalimumab, infliximab, and etanercept bind to the same target molecule, TNF-α, we analyzed the effects of binding with TNF-α on the affinity of these therapeutic proteins to FcRn. First, 0–2680 nM TNF-α was added to 335 nM infliximab and incubated for at least 1 h. The resulting mixture was then injected into the flow cell, and the affinities to FcRn were analyzed. By adding TNF-α, the shape of the sensorgram was drastically altered (Fig. 7*A*). The Abs (adalimumab and infliximab) can maximally bind to two TNF-α trimers, whereas etanercept binds to one TNF-α trimer. When the relative concentrations of TNF-α are low, three molecules of the Ab can bind to each TNF-α trimer, and cross-linked TNF/Ab complexes are formed (30). To evaluate the affinity

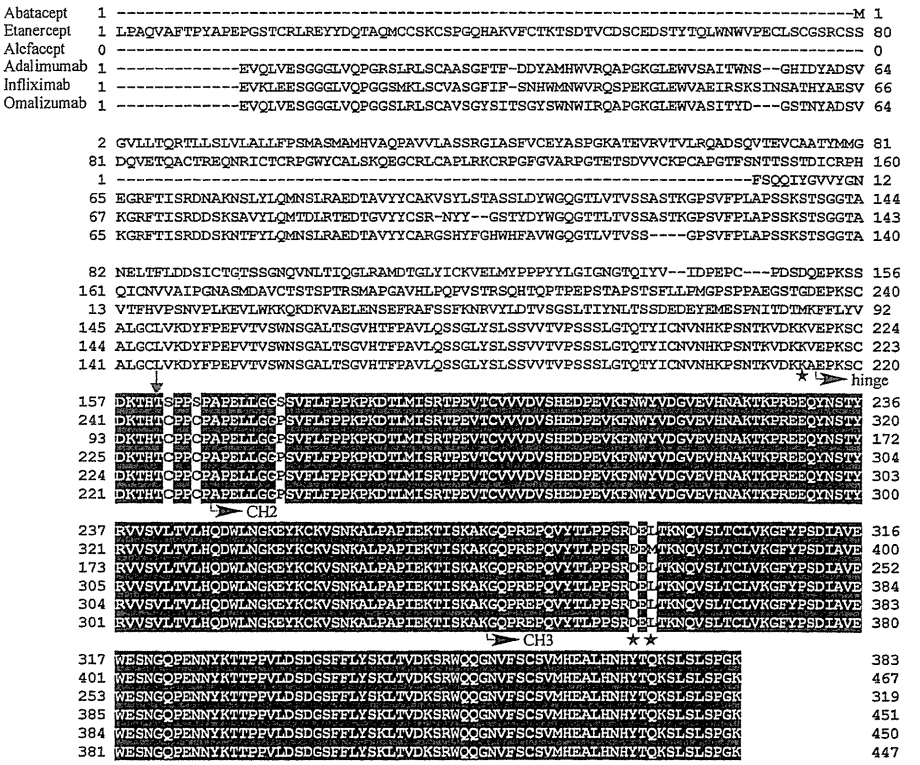

FIGURE 5. The amino acid sequences of abatacept, alefacept, etanercept, and H chains of adalimumab and infliximab. The amino acids marked with a star are different among allotypes of IgG1. The gray arrow is the cleavage site of IgG1 with papain (27). The amino acid sequences were obtained from the following links: abatacept, http://whqlibdoc.who.int/druginfo/18_2_2004_INN91.pdf; alefacept, http://whqlibdoc.who.int/druginfo/DRUG_INFO_14_4_2000_INN-84.pdf; etanercept, http://whqlibdoc.who.int/druginfo/DRUG_INFO_13_2_1999_INN-81.pdf; adalimumab, www.info.pmda.go.jp/shinyaku/g080405/10015900_22000AMX01598_A100_1.pdf; infliximab, www.info.pmda.go.jp/shinyaku/g020102/40031500_21400AMY00013_Q100_2.pdf; and omalizumab, www.drugbank.ca/drugs/DB00043.

between FcRn and TNF-α–binding proteins, excess TNF-α was added to adalimumab, infliximab, and etanercept (8-fold molar excess to 42–670 nM Abs and 4-fold to 168–2680 nM etanercept) to avoid forming nonuniform complexes. The sensorgrams were fitted by the bivalent analyte model (Fig. 7*B*). Although the fitted lines did not completely match the observed sensorgrams, the K_D values of infliximab, adalimumab, and etanercept to FcRn were calculated to be 2057, 1321, and 4286 nM, respectively (Fig. 7*C*). The affinity of infliximab–TNF-α complex or adalimumab–TNF-α complex was lower than that of infliximab or adalimumab, respectively (Fig. 7*C*). These results suggest that at least for these anti–TNF-α Abs, binding with target molecules decreases the affinity to FcRn. They may also suggest that the anti–TNF-α Abs complexed with TNF-α will be degraded more rapidly than anti–TNF-α Abs free from TNF-α in vivo.

Discussion

To our knowledge, this is the first article to elucidate the affinities of clinically used Fc domain-containing therapeutic proteins to FcRn in a comparative study. Because the affinities of these therapeutic proteins to FcRn were found to be highly correlated with the serum half-lives in humans, with the exception of infliximab, rituximab, and trastuzumab, the importance of FcRn in regulating the serum half-life of Fc domain-containing therapeutic proteins was suggested. The key observation was that the Fc-fusion proteins showed lower affinity to FcRn than Abs. These data provided us with one of the answers to the question of why the Fc-fusion proteins containing the Fc domain of human IgG1 exhibit a shorter half-life than human IgG1.

In the current study, we used the bivalent analyte model of BIAevaluation software. Most studies analyzing Fc-FcRn interactions have used the bivalent analyte model (15, 31) or the heterogeneous ligand model (7, 15, 31). Although the sensorgrams in our experiments were able to be fitted by both models, they were better fitted by the bivalent analyte model. Considering that two molecules of hFcRn bind to each IgG, resulting in a 2:1 binding stoichiometry (15), the bivalent analyte model seems to be suitable. It has been reported that the dual bivalent analyte model better fits the data of the FcRn-Fc interaction (32), although there are cases in which the bivalent analyte model does not work well. In the article about the dual bivalent analyte model, it was speculated that high-affinity and low-affinity types of FcRn existed on the surface of the BIAcore chip and that the low-affinity type receptor was probably an experimental artifact (32). Possibly because the content of the low-affinity type of FcRn on the chip is comparatively low in our immobilizing condition, the sensorgrams in our experiments might have been well-fitted by the bivalent analyte model.

Among the therapeutic proteins tested in this study, the Fc fusion proteins showed relatively lower affinities to FcRn (Figs. 2, 3), although the affinities to FcγRI are comparable to those of Abs (Fig. 4). Although the Fc domain binds to FcRn via the CH2-CH3 domain interface (33), the primary structures of the Fc domains of tested therapeutic proteins were almost the same, and cleavage of the Fc domains from Fab or the receptor region gave similar K_D values to FcRn (Fig. 6). These results suggest that the receptor regions of Fc-fusion protein alter the conformation of the FcRn-binding region (CH2-CH3 domain interface), not of the FcγRI-binding region (hinge proximal region of CH2 domain), or cause steric hindrance on the CH2-CH3 domain interface. The influence of regions besides the Fc domain on FcRn-binding regions would also be the case for Abs, as shown in Fig. 7.

Our results presented in this study can provide valuable information regarding the molecular design of novel Fc domain-containing therapeutic proteins and demonstrate the usefulness of FcRn-binding analysis in the characterization of Fc domain-containing therapeutic proteins. In addition to the Fc fusion proteins used in this study, rilonacept, a Fc-fusion protein consisting of ligand-binding domains of the extracellular portions of the human IL-1 receptor component (IL-1RI) and IL-1 receptor accessory protein linked to the Fc portion of human IgG1, and romiplostim,

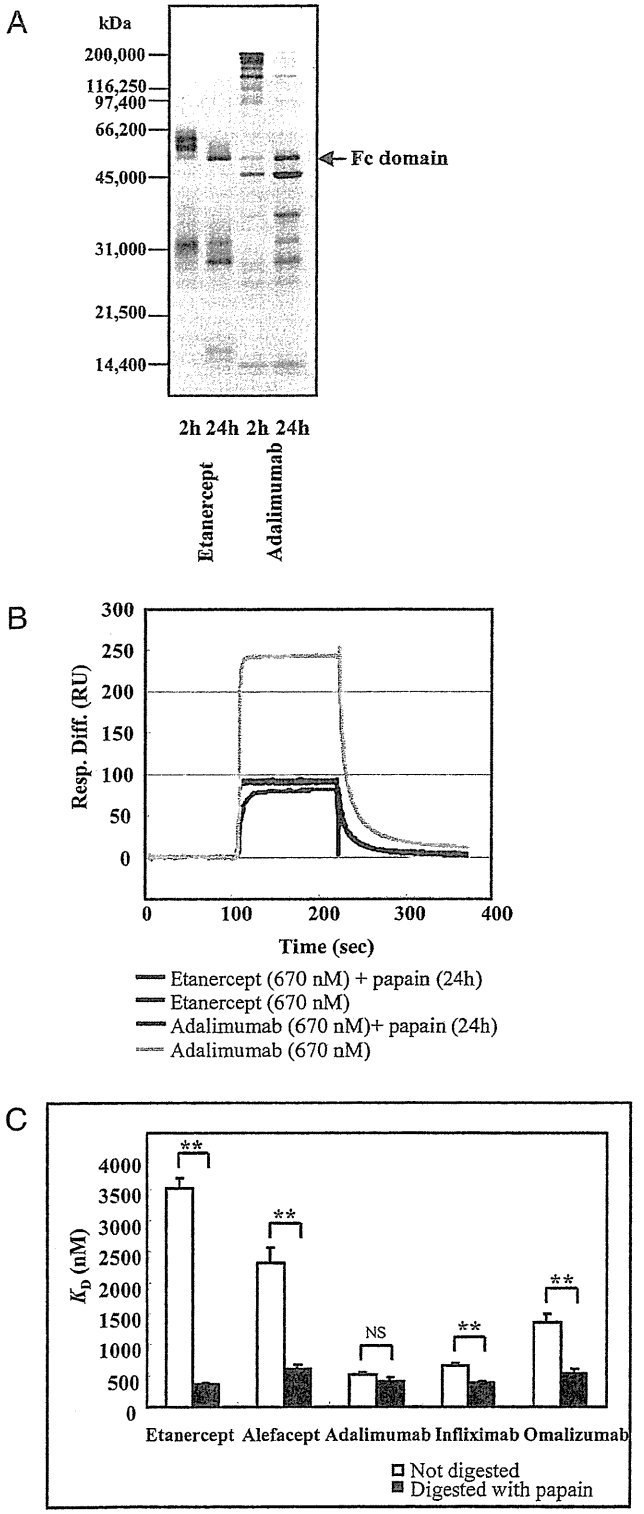

FIGURE 6. Effects of papain digestion on the affinities of Fc domain-containing therapeutic proteins to FcRn. *A*, The nonreduced SDS-PAGE of etanercept and adalimumab digested with papain for 2 and 24 h. *B*, The comparison between the sensorgrams of etanercept and adalimumab with or without papain digestion. *C*, Comparison of the affinity to FcRn among etanercept, alefacept, adalimumab, infliximab, and omalizumab, which were digested or not digested with papain. The K_D values were calculated from the sensorgrams at the range of concentrations described as follows. The concentrations of papain-digested etanercept, papain-digested alefacept, adalimumab, papain-digested adalimumab, infliximab, papain-digested infliximab, and papain-digested omalizumab were 42–670 nM; those of etanercept and alefacept were 168–5360 nM, and those of omalizumab were 42–1340 nM. Each bar shows the average K_D value + SD, which was calculated from three independent experiments. $^{**}p < 0.01$. NS, no significant difference according to Student *t* test.

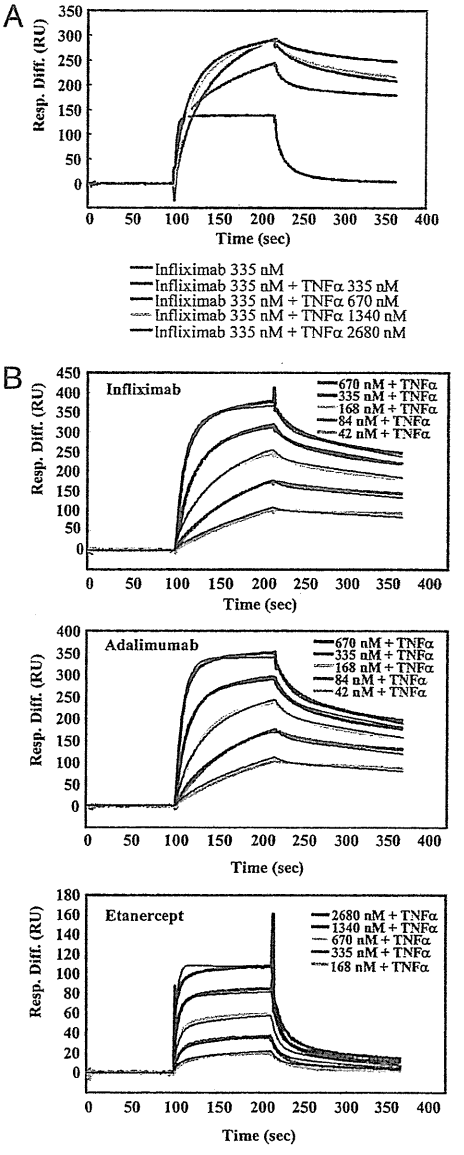

C

	Affinity to FcRn K_D (nM)	
	control	preincubate with TNFα
Etanercept	3705	4286
Adalimumab	673	1321
Infliximab	751	2057

FIGURE 7. Effects of binding with the target molecules on the affinities of Fc domain-containing therapeutic proteins to FcRn. *A*, The sensorgrams of infliximab (335 nM) preincubated with TNF-α (0–2680 nM). *B*, The sensorgrams of infliximab (*upper panel*), adalimumab (*middle panel*), and etanercept (*lower panel*) preincubated with TNF-α (8-fold molar excess to 42–670 nM Abs and 4-fold to 168–2680 nM etanercept). The sensorgrams were fitted by the bivalent analyte model. *C*, The K_D values calculated from the sensorgrams shown in *B*. The values of infliximab, adalimumab, and etanercept derived from the same series of experiments are also shown as controls.

a Fc-peptide fusion protein consisting of human IgG1 Fc domain linked at the C terminus to a peptide containing two thrombopoietin receptor-binding domains, were approved recently (34, 35). The